THE ASTROPHYSICAL JOURNAL, 545:603–624, 2000 December 20

IONIZED GAS IN DAMPED Lyα PROTOGALAXIES. II. COMPARISON BETWEEN MODELS AND THE KINEMATIC DATA

ARTHUR M. WOLFE[1]
Department of Physics, and Center for Astrophysics and Space Sciences, University of California at San Diego, C-0424, La Jolla, CA 92093; awolfe@ucsd.edu

AND

JASON X. PROCHASKA[1]
The Observatories of the Carnegie Institute of Washington, 813 Santa Barbara Street, Pasadena, CA 91101; xavier@ociw.edu
Received 2000 May 24; accepted 2000 August 8

ABSTRACT

We test semianalytic models for galaxy formation with accurate kinematic data of damped Lyα protogalaxies presented in a companion paper. The models envisage centrifugally supported exponential disks at the centers of dark matter halos, which are filled with ionized gas undergoing radial infall to the disks. The halo masses are drawn from cross section weighted mass distributions predicted by cold dark matter (CDM) cosmogonies, or by the null hypothesis that the dark matter mass distribution has not evolved since $z \sim 3$ (i.e., the Tully-Fisher [TF] models). In our models, C IV absorption lines detected in damped Lyα protogalaxies arise in infalling ionized clouds, while the low-ion absorption lines arise from neutral gas in the disks. Using Monte Carlo methods, we find that: (1) The CDM models are incompatible with the low-ion statistics at more than 99% confidence, whereas some TF models cannot be ruled out at more than 88% confidence. (2) Both CDM and TF models are in general agreement with the observed distribution of C IV velocity widths. (3) The CDM models generate differences between the mean velocities of C IV and low-ion profiles that are compatible with the data, while the TF model produces differences in the means that are too large. (4) Both CDM and TF models produce ratios of C IV to low-ion velocity widths that are too large. (5) Neither CDM nor TF models generate C IV versus low-ion cross-correlation functions compatible with the data. While it is possible to select model parameters resulting in agreement between the models and the data, the fundamental problem is that the disk-halo configuration assumed in both cosmogonies does not produce significant overlap in velocity space between C IV and low-ion velocity profiles. We conjecture that including the angular momentum of the infalling clouds will increase the overlap between C IV and low-ion profiles.

Subject headings: galaxies: evolution — galaxies: ISM — quasars: absorption lines

1. INTRODUCTION

This is the second of two papers that discuss ionized gas in damped Lyα systems. In Paper I (Wolfe & Prochaska 2000) we presented velocity profiles drawn from a sample of 35 damped Lyα systems for the high ions C IV and Si IV, and the intermediate ion Al III. Comparison among these profiles and with profiles previously obtained for low ions such as Fe II showed the damped Lyα systems to consist of two distinct kinematic subsystems: a low-ion subsystem composed of low and intermediate ions, and a high-ion subsystem containing only high ions. The evidence distinguishing between the kinematic subsystems is robust and stems from a battery of tests comparing distributions of various test statistics. It also stems from differences between the C IV versus low-ion or C IV versus Al III cross-correlation functions on the one hand, and the C IV versus Si IV or Al III versus low-ion cross-correlation functions on the other. While the latter have high amplitude and small velocity width, the former have lower amplitude and wider velocity width. This is because velocity profiles of ions arising in the same kinematic subsystem comprise narrow velocity components that line up in velocity space, whereas velocity components arising from ions in different kinematic subsystems are misaligned in velocity space. However, the existence of a statistically significant C IV versus low-ion cross-correlation function suggests that the two subsystems are interrelated. This is also indicated by a systematic effect in which the C IV profile velocity widths, $\Delta v_{\rm C\,IV}$, are greater than or equal to the low-ion profile velocity widths, $\Delta v_{\rm low}$, in 29 out of 32 systems.

In Paper I we claimed that these phenomena indicate that the two subsystems are located in the same gravitational potential well. In this paper we expand on this idea with specific models. The models assume that the low-ion subsystems are centrifugally supported disks of neutral gas located at the centers of dark matter halos (see Mo, Mao, & White 1998; hereafter MMW), whereas the high-ion subsystems comprise photoionized clouds undergoing infall from a gaseous halo to the disk. That is, we assume that the dark matter halos contain hot virialized gas in pressure equilibrium with the photoionized clouds. The hot gas undergoes a subsonic cooling flow toward the disk, while the denser clouds infall at velocities approaching free fall (Mo & Miralda-Escudé 1996; hereafter MM). The models are set in a cosmological context by computing the mass distribution and other properties of the dark matter halos using Press-Schechter theory and the cold dark matter (CDM) cosmogonies adopted by semianalytic models for galaxy formation. We also consider the null hypothesis that

[1] Visiting Astronomer, W. M. Keck Telescope. The Keck Observatory is a joint facility of the University of California and the California Institute of Technology.

galaxies at $z \approx 3$ have the same dynamical properties as nearby galaxies (this model, the Tully-Fisher [TF] model, is defined in § 2.4.2).

We test the models using a Monte Carlo technique for computing absorption spectra arising when sight lines that randomly penetrate intervening disks also intercept ionized clouds in the halo. Section 2 presents models for the neutral gas. We discuss properties of the disk, the cosmological framework, and Monte Carlo techniques. In § 3 we discuss models for the ionized gas. We derive expressions for the structure and kinematics of the two-phase halo gas. Expressions for C IV column densities of the clouds are derived. In § 4 we give results of the Monte Carlo simulations for the low-ion gas for both CDM and TF models. Results of Monte Carlo simulations for the ionized gas are given in § 5. Here we also consider tests of correlations between the kinematics of the high and low ions. In § 6 we investigate how the results of § 5 are affected by changes in some key parameters, such as central column density and low-end cutoff to the input dark matter halo mass distribution. Concluding remarks are given in § 7.

2. MODELS OF THE NEUTRAL GAS

2.1. *Cosmological Framework*

To place the model in a cosmological context, we assume that bound dark matter halos evolve from linear density contrasts, $\delta(x, t) \equiv \delta\rho/\rho$, according to gravitational instability theory for Friedmann cosmologies (Peebles 1980). We consider adiabatic CDM models (ACDM) in which δ_k, the Fourier transforms of $\delta(x, t)$, are Gaussian distributed with a variance given by $P(k)$, the power spectrum at the epoch of radiation and matter equality. We also consider isocurvature CDM models (ICDM) in which the δ_k are not Gaussian distributed (Peebles 1999b). The δ_k, or more specifically, the rms density contrasts in spheres with mass scale M, i.e., Δ_M, grow with time until they go nonlinear and collapse. According to the spherical collapse model, this occurs when the Δ_M predicted by linear theory equals $\delta_c = 1.68$. To compute $n(M, z)dM$, the density of bound halos in the mass interval $(M, M + dM)$, we follow previous authors (e.g., MMW) who used the Press-Schecter formalism in the case of ACDM. In Appendix A we derive an expression for $n(M, z)dM$ in the case of ICDM.

We also test the null hypothesis that little or no evolution of galaxies has occurred since the epochs of damped Lyα absorption; that is, a hypothesis assuming that current disks, with higher ratios of gas to stars, were in place at $z > 3$. This scenario resembles the semianalytic models in that we assume that centrifugally supported disks reside at the centers of dark matter halos filled with hot gas at the virial temperatures. However, we do not assume a CDM power spectrum or the Press-Schecter formalism to compute the mass distribution of halos. Rather, we assume that (1) the luminosity function of galaxies in the redshift range of the damped Lyα sample in paper I, i.e., $z = [2, 5]$, is given by the Schecter function determined from nearby galaxies (e.g., Loveday, Tresse, & Maddox 1999); (2) galaxies at these redshifts obey the same Tully-Fisher relationship between luminosity and rotation speed as at $z = 0$; and (3) a correlation between disk radial scale length and disk rotation speed exists. This model, hereafter referred to as TF, is an extension of the rapidly rotating disk model suggested by Prochaska & Wolfe (1997, 1998; hereafter PW97 and PW98, respectively). We describe this model in more detail in the following sections.[2]

Throughout the paper, we compare results for the TF model and four CDM cosmogonies. The cosmological settings of the CDM models are specified by (1) the current total matter density, Ω_M; (2) the cosmological constant, Ω_Λ; (3) the Hubble constant, h, where $h = H_0/100$ km s^{-1} Mpc^{-1}; (4) σ_8, the rms linear density contrast at $z = 0$ in spheres of radius 8 h^{-1} Mpc; and (5) n, the power-law index for the power spectrum, in cases where $P(k) \propto k^n$. The values of the parameters are given in Table 1. The SCDM, ΛCDM, and OCDM are normal ACDM models. In all three cases, $P(k)$ is given by the Bardeen et al. (1986) expression (which is not a power law). In the ICDM model, we follow Peebles by assuming $P(k) \propto k^n$ and $n = -1.8$. The cosmological parameters specifying the TF model are also given in Table 1.

2.2. *Disk Models*

Most semianalytic models assume that the neutral gas causing damped Lyα absorption is confined to centrifugally supported disks at the centers of dark matter halos (e.g., Kauffmann 1996; MMW). The spherical collapse model is used to define the limiting virial radius as r_{200}, the radius within which the mean density of dark matter equals $200\rho_{\rm crit}(z)$, where $\rho_{\rm crit}(z)$ is the critical density of the universe at redshift z. Thus, V_{200}, the circular velocity at r_{200}, is related to r_{200} and M, the halo mass within r_{200}, by

$$V_{200} = [10GH(z)M]^{1/3}\,, \quad r_{200} = \frac{V_{200}}{10H(z)}\,, \tag{1}$$

where $H(z)$ is the Hubble parameter, $(a^{-1}da/dt)$, at z. MMW also define m_d and j_d as the fractions of halo mass, M, and angular momentum, J, in disk baryons. Assuming the halos to be singular isothermal spheres embedding disks having exponential surface density profiles with radial scale lengths $R_d^{\rm iso}$, they find that

$$\begin{aligned} R_d^{\rm iso} &= \frac{1}{\sqrt{2}}\,\frac{j_d}{m_d}\,\lambda r_{200} \\ &\approx 8.8\ h^{-1}\ {\rm kpc}\left(\frac{\lambda}{0.05}\right)\left(\frac{V_{200}}{250\ {\rm km\ s^{-1}}}\right) \\ &\quad \times \left[\frac{H(z)}{H_0}\right]^{-1}\left(\frac{j_d}{m_d}\right), \end{aligned} \tag{2}$$

and

$$\begin{aligned} N_0^{\rm iso} &= 4.8 \times 10^{22}\ h\ {\rm cm^{-2}}\,\frac{m_d}{0.05}\left(\frac{\lambda}{0.05}\right)^{-2} \\ &\quad \times \frac{V_{200}}{250\ {\rm km\ s^{-1}}}\,\frac{H(z)}{H_0}\left(\frac{m_d}{j_d}\right)^2, \end{aligned} \tag{3}$$

[2] We could have adopted luminosity functions that are *measured* in this redshift interval. The most accurate determinations are for the Lyman-break galaxies (Steidel et al. 1999). However, we rejected this procedure because the rotation speeds of these objects have not been measured, nor is it known whether or not they contain rotating disks. The strong clustering exhibited by the Lyman-break galaxies suggests otherwise. Nevertheless, we briefly discuss this possibility in § 6.2.

TABLE 1

MODEL PARAMETERS

Parameter	SCDM	ΛCDM	OCDM	ICDM	TF
Ω_M	1.0	0.3	0.2	0.2	0.3
Ω_Λ	0.0	0.7	0.0	0.8	0.7
h	0.5	0.7	0.7	0.7	0.7
σ_8	0.6	1.0	1.03	0.9	...
n	[a]	[a]	[a]	−1.8	...

[a] CDM power spectrum given by Bardeen et al. (1986) expression.

where the spin parameter of the halo $\lambda = J|E|^{1/2}G^{-1}M^{-5/2}$ (where E is the total energy of the halo), and N_0 is the central H I column density perpendicular to the disk. The distribution of λ is given by

$$p(\lambda)d\lambda = \frac{1}{\sqrt{2\pi}\sigma_\lambda}\exp\left[-\frac{\ln^2(\lambda/\langle\lambda\rangle)}{2\sigma_\lambda^2}\right]\frac{d\lambda}{\lambda}, \quad (4)$$

where the mean and dispersion are determined from numerical simulations to be $\langle\lambda\rangle = 0.05$ and $\sigma_\lambda = 0.5$ (see Barnes & Efstathiou 1987).

For the TF models, we infer the parameters of the halo from observed properties of the disk. Thus, we use model rotation curves to infer V_{200} from $V_{\max}$, the observed maximum rotation speed (see below). We then use equation (1) to obtain the mass and virial radius of the halo. In this case, we obtain the radial scale length and central column density of the disk by adopting the following correlations inferred by MMW from the spiral galaxy data of Courteau (1996, 1997):

$$R_d^{\rm Cor} = -1.25 + 7.4\left(\frac{V_{\max}}{250\ {\rm km\ s^{-1}}}\right)h^{-1}\ {\rm kpc}, \quad (5)$$

$$N_0^{\rm Cor} = 3.6\times 10^{22+0.45(V_{\max}/250\ {\rm km\ s^{-1}})}\mu^{-1}\ h\ {\rm cm^{-2}}, \quad (6)$$

where μ is the mean molecular weight of the gas.

2.3. *Rotation Curves*

We next turn to the mass distribution of the halo. This is crucial for determining both the rotation curve of the disk and the dynamics of gaseous infall discussed in § 3. For our model, we adopt the analytical fit to the halo mass distribution found in the N-body simulations of Navarro, Frenk, & White (1997; hereafter NFW). In this case the halo rotation curve, defined by $V_{\rm rot}(r) \equiv [GM(r)/r]^{1/2}$, has the form

$$V_{\rm rot}(r) = V_{200}\sqrt{\frac{c}{x}\frac{\ln(1+x)-x/(1+x)}{\ln(1+c)-c/(1+c)}}, \quad x = \frac{r}{r_s}, \quad (7)$$

where the concentration parameter $c \equiv r_{200}/r_s$, and at $r = r_s$ the halo mass density $\rho \propto r^{-2}$. NFW developed a self-consistent theory in which c depends on V_{200} and redshift, z, in the sense that at a given z, c declines with increasing V_{200}, and at a given V_{200}, c decreases with z. We use the algorithms described in NFW to compute $c = c(z, V_{200})$. NFW halo rotation curves corresponding to $z = 2.5$, $\lambda = 0.05$, $m = 0.05$, and the ΛCDM cosmology appear as solid curves in Figure 1 for $V_{200} = 50$–250 km s^{-1}. As expected, $V_{\rm rot} = V_{\max}$ at $r \approx 2r_s$. Curves with lower V_{200} appear to rise more rapidly in the interval $r = [0, r_{200}]$ because the ratio r_s/r_{200} decreases with decreasing V_{200}.

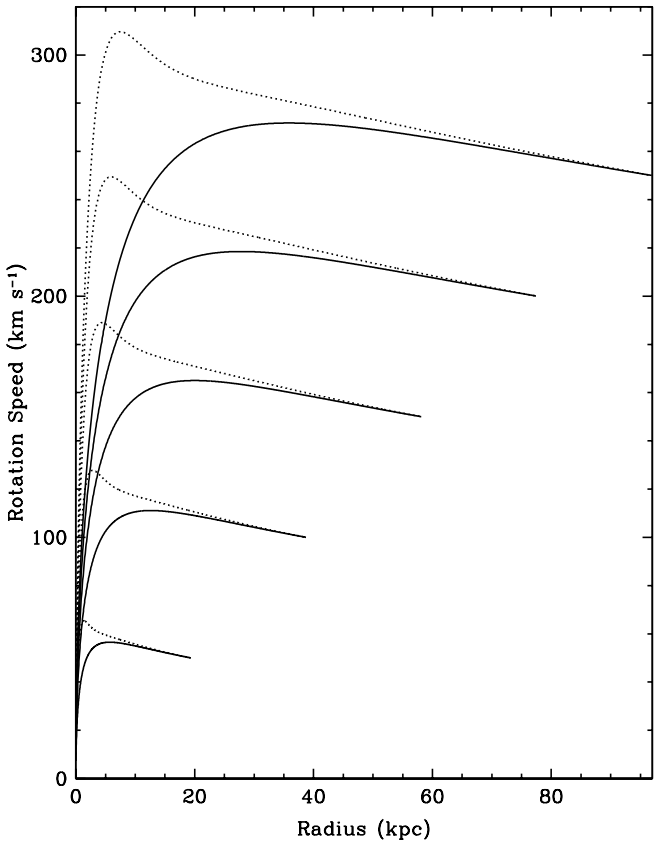

FIG. 1.—NFW rotation curves corresponding to $z = 2.5$, $\lambda = 0.05$, $m = 0.05$, and the ΛCDM cosmology. Solid curves show halo rotation curves from eq. (9) corresponding to $V_{200} = 50$, 100, 150, 200, and 150 km s^{-1}. Dotted curves show rotation curves resulting from modifications due to adiabatic contraction and disk self-gravity. Curves are plotted out to r_{200}

However, the expression for the halo $V_{\rm rot}(r)$ in equation (7) is incomplete, since it ignores the presence of the disk. Self-gravity of the disk affects the mass distribution of the halo through adiabatic contraction (Blumenthal et al. 1986). We used the MMW formalism to compute rotation curves due to contracted halos and found that $V_{\rm rot}(r)$ differed from the expression in equation (7) by less than ≈15%. Given the uncertainties in the models, we ignore these corrections and use the halo mass distribution implied by equation (7) when computing dynamics of *infall*.

On the other hand, the rotation curve of the *disk* can differ significantly from equation (7) when the disk contribution to the net potential gradient is added to that of the contracted halo. MMW compute the scale length and central column density of centrifugally supported exponential disks in adiabatically contracted NFW halos formed by spherical collapse. In comparison with halos modeled as singular isothermal spheres, they find

$$R_d^{\rm MMW} = R_d^{\rm iso}\ f_c^{-1/2}\ f_R, \quad N_0^{\rm MMW} = N_0^{\rm iso}\ f_c\ f_R^{-2}. \quad (8)$$

Explicit expressions for the functions f_c and f_R are given by MMW. They then use the new disk parameters to calculate the modified $V_{\rm rot}(r)$ for disks embedded in NFW halos. Examples of modified $V_{\rm rot}(r)$ corresponding to $\lambda = 0.05$, $m_d = 0.05$, and $z = 2.5$ are shown as dotted curves in Figure 1. Clearly, the rotation speeds sampled by sight lines traversing these model disks lie between V_{200} and $f_V V_{200}$, the

maximum of the modified disk rotation curve, where f_V, a function tabulated by MMW, exceeds unity. Given the wide range of possible rotation curves appropriate for model damped Lyα systems (see PW98), we assume that the *disk* rotation curves have either of the following constant speeds:

$$V_{\rm rot}(r) = V_{200} \times \begin{cases} 1 \\ f_V \end{cases}, \tag{9}$$

For the TF models, V_{200} is not given a priori. Rather, we assume $V_{\rm rot}(r) = V_{\rm max}$ and that $V_{\rm max}$ is selected from an empirical distribution derived from the TF relation (see § 2.4.2). The radial scale length and central column densities then follow from equations (5) and (6). In this case, $V_{200} = V_{\rm max}$ or $V_{200} = V_{\rm max}/f_V$.

2.4. *Monte Carlo Models*

In previous work (PW97, PW98) we tested models by comparing predicted and empirical distributions of the four test statistics for the low ions (Fig. 6 in Paper I). The model distributions were computed by a Monte Carlo technique in which low-ion absorption profiles were produced by sight lines traversing 10,000 randomly oriented disks, and test statistics were determined for each profile. In PW97, the disk models were based on the simplifying assumption of *identical* disks with flat rotation curves characterized by a single rotation speed, while in PW98 more realistic forms of $V_{\rm rot}(r)$ were used for the identical disks. Here we extend this approach to account for the distributions of halo masses and spin parameters.

2.4.1. *CDM*

MMW give an expression for the cumulative probability that sight lines to the background QSOs intercept disks in halos with masses exceeding that corresponding to $V_{\rm max}$: the result is averaged over $p(\lambda)$. For the Monte Carlo model, we require the differential expression; that is, the probability for intercepting disks in the spin parameter interval (λ, $\lambda + d\lambda$), circular velocity interval (V_{200}, $V_{200} + dV_{200}$), and redshift interval (z, $z + dz$). The result is given by

$$\begin{aligned} dP_{\rm CDM}(z, \lambda, V_{200}) = & \left[dz \, \frac{\pi}{2} (1+z)^3 \left(-c \, \frac{dt}{dz} \right) \right] \\ & \times d\lambda p(\lambda) [R_d^{\rm iso}(V_{200}, \lambda, z) N_0^{\rm iso}(V_{200}, \lambda, z)]^2 \\ & \times dV_{200} \, n(V_{200}, z) F(N_0^{\rm iso}) , \end{aligned} \tag{10}$$

where

$$F(N_0^{\rm iso}) = \times \begin{cases} \dfrac{1}{(N_0^{\rm iso})^2} \left[\dfrac{1}{2} + \ln\left(\dfrac{N_0^{\rm iso}}{N_l} \right) \right] \left[1 + \ln\left(\dfrac{N_0^{\rm iso}}{N_l} \right) \right] & N_0^{\rm iso} > N_l , \\ \dfrac{1}{2N_l^2} & N_0^{\rm iso} < N_l , \end{cases} \tag{11}$$

and

$$n(V_{200}, z) = n(M, z) \left| \frac{dM}{dV_{200}} \right| . \tag{12}$$

Here $N_l = 2 \times 10^{20}$ cm^{-2} is the threshold column density for damped Lyα surveys (e.g., Wolfe et al. 1995).

For given redshift intervals and cosmologies, the function $dP_{\rm CDM}$ describes a surface above the (λ, V_{200}) plane. To form synthetic samples of 10,000 low-ion profiles, we randomly draw (λ, V_{200}) pairs according to the height of the surface above the plane. To assure compliance with the damped Lyα surveys, sight lines resulting in observed H I column densities less than N_l are thrown out. We restrict the boundaries of the surface to $V_{200} < 300$ km s^{-1} to insure that gas in virialized halos has ample time to cool and collapse to the disk (e.g., Rees & Ostriker 1977) by redshift $z = 2.6$, the median redshift of the kinematic sample. We also assume that $dP_{\rm CDM}$ cuts off below $V_{200} = 30$ km s^{-1}, since gas photoionized to temperatures of $\sim 10^4$ K by the UV background radiation escapes from dark matter halos with $V_{200} < 30$ km s^{-1} (Thoul & Weinberg 1995; Navarro & Steinmetz 1997; Kepner, Babul, & Spergel 1997; we investigate the consequences of modifying this restriction in § 6). Figure 2 shows the resulting distributions of V_{200} for all the CDM models in Table 1. All the CDM curves exhibit maxima near the V_{200} cutoff predicted by hierarchical cosmologies, and as predicted, the curves decline with increasing V_{200}. As expected, the largest fraction of massive halos is indicated for the ICDM models. Thereafter, the fraction decreases progressively from OCDM, to ΛCDM, to SCDM adiabatic models.

2.4.2. *TF*

The curve labeled TF in Figure 2 represents the null hypothesis discussed above. In this case, the x-axis corresponds to $V_{\rm max}$ rather than V_{200}. This is because V_{200} is a theoretical construct, whereas the null hypothesis is based

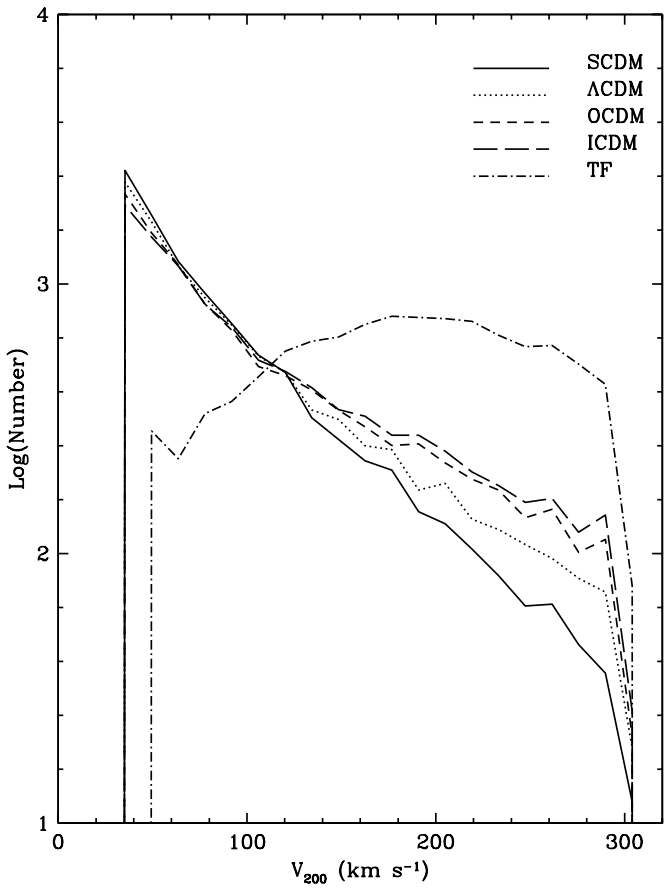

FIG. 2.—Input circular velocity distributions for the CDM and TF models used in Monte Carlo simulations. Computed as described in the text for the velocity interval (30, 300) km s^{-1}. The abscissa corresponds to V_{200} in CDM and $V_{\rm max}$ in TF models.

only on the *observed* properties of current galaxies. The crucial relationship here is the Tully-Fisher equation that connects L and $V_{\rm max}$, i.e.,

$$L(V_{\rm max}) = L_*(V_{\rm max}/V_*)^{\gamma}\,, \tag{13}$$

where V_* is $V_{\rm max}$ for a galaxy with luminosity $L = L_*$. With the last equation, we can obtain expressions for the interception probability,

$$dP_{\rm TF}(z, V_{\rm max}) = \left[dz\,\frac{\pi}{2}\,(1+z)^3\left(-c\,\frac{dt}{dz}\right)\right] \times [R_d^{\rm Cor}(V_{\rm max}, z)N_0^{\rm Cor}(V_{\rm max}, z)]^2 \times dV_{\rm max}\,n(V_{\rm max}, z)F(N_0^{\rm Cor})\,, \tag{14}$$

where $dV_{\rm max}\,n[L(V_{\rm max})]$ is the present density of galaxies with maximum rotation velocities in the interval ($V_{\rm max}$, $V_{\rm max} + dV_{\rm max}$), and $F(N_0^{\rm Cor})$ is given by equation (11), with $N_0^{\rm Cor}$ substituted for $N_0^{\rm iso}$. To determine $n[L(V_{\rm max})]$, we assume a Schecter luminosity function; i.e.,

$$dV_{\rm max}\,n(V_{\rm max}, z) = \Phi_*(L/L_*)^{-\alpha}\exp(-L/L_*)d(L/L_*)\,. \tag{15}$$

The TF curve depends on the parameters α, γ, and V_*, for which we assumed values of 1.0, 3.0, and 250 km s^{-1}, respectively. These are representative for the values of parameters adopted by Gonzalez et al. (2000), who computed $n(V_{\rm max}, 0)$. They analyzed data sets from extensive surveys carried out at B magnitudes. However, using Cepheid calibrated galaxies, Sakai et al. (2000) derive TF relations indicating lower values of V_* ($\approx$180 km s^{-1}) for the B-magnitude TF relation. Low values of V_*, as well as higher values of γ, are indicated by their I-band TF relation, and from similar relations found by Giovanelli et al. (1997). In § 6 we discuss the sensitivity of our results to these parameters. The point we wish to emphasize is that for acceptable ranges of these parameters, the TF curve differs from the CDM curves in that it (1) peaks at $V_{\rm max} \approx V_*/2 \approx$ 130 km s^{-1}, which is large compared to the 30 km s^{-1} peak of the CDM curves; (2) has little power near the latter peak; and (3) falls off exponentially when $V_{200} > V_*/2$. Of course, the comparison with CDM is inexact, since $P_{\rm CDM}$ depends on V_{200}, while $P_{\rm TF}$ depends on $V_{\rm max}$. Still, the differences between V_{200} and $V_{\rm max}$ are not large enough to invalidate these conclusions.

3. IONIZED GAS

Assume that disks arise from the infall of ionized gas predicted to fill dark matter halos. According to the MM model, the halo gas is accreted during merger events with other halos and is shock-heated to the virial temperature of the halo, $kT_{\rm vir} \equiv (1/2)(\mu m_{\rm H} V_{200}^2)$; we assume $\mu = 0.4$. The duration of the accretion phase is presumably short compared to t_M, the time interval between events. For the mass interval corresponding to $V_{200} = [30, 300]$ km s^{-1}, $T_{\rm vir}$ ranges between 3×10^4 and 3×10^6 K. In the case of massive halos, the cooling time, $t_{\rm cool}$, exceeds the age of the gas, t_M, at $r = r_{200}$. Because the density of the gas increases with decreasing radius, $t_{\rm cool}$ decreases with decreasing radius until $t_{\rm cool} = t_M$ at the cooling radius, $r_{\rm cool}$. At $r < r_{\rm cool}$ the gas moves radially inward in a quasi-static cooling flow (Fabian 1994). Cool clouds form in pressure equilibrium with the hot gas, since the hot gas is thermally unstable. Due to the loss of buoyancy, the denser clouds fall inward at speeds determined by the imbalance between gravity and ram pressure. Because of rapid cooling, most of the gas in lower mass halos cools before moving inward, but within a limited range of halo masses there is always hot low-density gas left over, which also moves inward in a cooling flow and exerts pressure on cooler clouds that have formed. The MM hypothesis is that the cool clouds are photoionized by background UV radiation and that they are the sites of C IV absorption lines in QSO absorption systems. Here we extend this hypothesis to model the ionized gas causing C IV absorption in damped Lyα systems.

3.1. *Two-Phase Structure of the Halo Gas*

Following MM, we assume that the hot gas is in hydrostatic equilibrium with the dark matter potential and that it exhibits adiabatic temperature and density profiles out to $r_{\rm min} = \min(r_{\rm cool}, r_{200})$. At $r > r_{\rm min}$, the hot gas either follows isothermal profiles, when $r_{200} > r_{\rm cool}$, or does not exist, when $r_{200} < r_{\rm cool}$. In Appendix B we derive expressions for $r_{\rm cool}$, and for $\rho_h(r)$ and $T_h(r)$, the density and temperature profiles, respectively, for hot gas in halos corresponding to the unmodified NFW rotation curves in equation (7). Examples of pressure profiles for high- and low-mass halos are shown in Figure 3. The figure shows the gas pressure in high-mass halos to be 10–100 times higher than in low-mass halos. The high pressures are mainly due to the higher virial temperatures of massive halos.

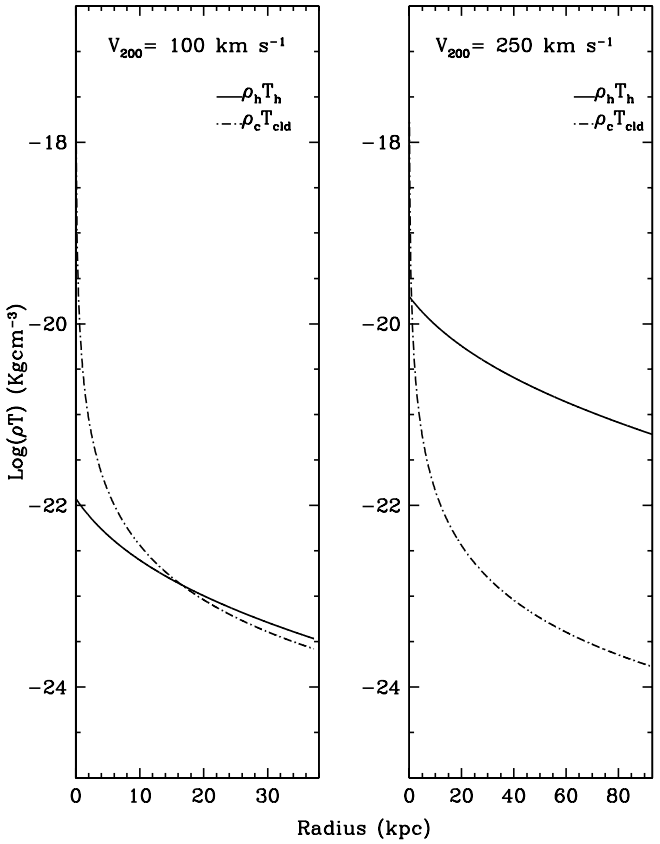

FIG. 3.—*Solid curves*: Pressure profiles for hot gas in halos with V_{200} = 100 (*left*) and 250 km s^{-1} (*right*). Pressure profiles are given by product of $\rho(r)_h$ and $T_h(r)$, the density and temperature, respectively, of the hot gas. Profiles are computed according to prescription in Appendix B. *Dot-dashed curves*: Smooth density of cool gas times temperature of clouds; i.e., $\rho_c\,T_{\rm cld}$. When latter exceeds pressure of hot gas, pressure equilibrium between cool clouds and hot gas breaks down (see § 4.1).

Gas in the cool phase comprises identical uniform spherical clouds with mass $M_{\rm cld}$, radius $R_{\rm cld}$, temperature $T_{\rm cld}$, and internal density $\rho_{\rm int}$. We adopt the MM model by assuming that clouds form at $r = r_{\rm min}$ with mass $M_{\rm cld}(r_{\rm min}) = 4 \times 10^5\ M_\odot$, and temperature $T_{\rm cld} = 2 \times 10^4$ K, since they are assumed to be photoionized. To compute $R_{\rm cld}$, MM assume that $\rho_{\rm int}$ is set by pressure equilibrium with the surrounding hot gas; i.e., $\rho_{\rm int} = \rho_h\, T_h/T_{\rm cld}$. However, this assumption is incorrect for a wide range of halo masses and radii. Specifically, pressure equilibrium breaks down when the pressure is sufficiently low for $R_{\rm cld}$ to equal the mean distance separating clouds. This will occur when $\rho_c(r)$, the average density of cool gas, exceeds $\rho_{\rm int}(r)$; i.e., when $\rho_c\, T_{\rm cld} > \rho_h\, T_h$. According to MM, $\rho_c(r)$ is given by

$$\rho_c(r) = \frac{C_1}{r^2}\,, \tag{16}$$

where the constant C_1 is evaluated in Appendix C. Figure 3 demonstrates how $r_{\rm cross}$, the radius at which $\rho_c\, T_{\rm cld} = \rho_h\, T_h$, decreases with increasing V_{200}. In Figure 4 we plot $r_{\rm cross}$, $r_{\rm cool}$, and r_{200} versus V_{200} for a ΛCDM cosmology, NFW halos, and $z = 2.5$ (we also plot the cooling radius of a singular isothermal sphere, $R_{\rm cool}$, for comparison with NFW halos). The point of the figure is to show that (1) pressure equilibrium breaks down throughout halos with $V_{200} < 100$ km s^{-1}, (2) pressure equilibrium breaks down only near the centers of halos with $V_{200} > 100$ km s^{-1}, (3) $r_{\rm min} = r_{200}$ for halos with $V_{200} < 250$ km s^{-1}, and (4) $r_{\rm min} = r_{\rm cool}$ for halos with $V_{200} > 250$ km s^{-1}. These trends are qualitatively similar for all the background cosmologies in Table 1.

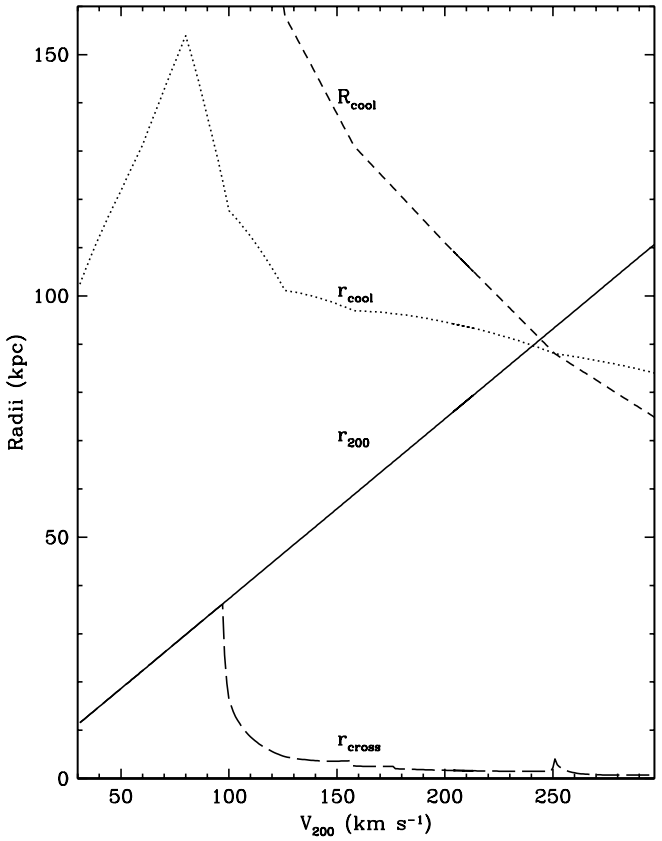

FIG. 4.—Critical radii vs. V_{200} for ΛCDM cosmology, NFW halos, and $z = 2.5$. $R_{\rm cool}$, the cooling radius of an infinite isothermal sphere, is computed from eq. (B7), and $r_{\rm cool}$, the cooling radius of a NFW halo, is computed from eq. (B6). The "virial radius" r_{200} is computed from eq. (3). The crossing radius, $r_{\rm cross}$, computed from eq. (C8), is the radius within which pressure equilibrium breaks down. Note that $r_{\rm min} = \min(r_{200}, r_{\rm cool})$ for values of V_{200} where $r_{\rm cross} \le r_{200}$. At $V_{200} < 100$ km s^{-1}, $r_{\rm min} = r_{\rm cross} = r_{200}$ (see § 4.2).

In order to compute the structure of the cool clouds, we assume $\rho_{\rm int} = \rho_c$ at $r < r_{\rm cross}$. As a result,

$$\rho_{\rm int}(r) = \begin{cases} \dfrac{\rho_h(r) T_h(r)}{T_c} & r > r_{\rm cross}\,, \\ \rho_c(r) & r < r_{\rm cross}\,. \end{cases} \tag{17}$$

The cross section of the infalling clouds is then given by

$$A(r) = \pi \left[\frac{3M_{\rm cld}(r)}{4\pi}\right]^{2/3} \begin{cases} \left[\dfrac{T_c}{T_h(r)\rho_h(r)}\right]^{2/3} & r > r_{\rm cross}\,, \\ \left[\dfrac{1}{\rho_c(r)}\right]^{2/3} & r < r_{\rm cross}\,, \end{cases} \tag{18}$$

which will be smaller than the value computed from pressure equilibrium at $r < r_{\rm cross}$. At $r > r_{\rm cross}$, $M_{\rm cld}$ is assumed to be a function of r, since the clouds may sweep up hot gas as they fall inward (see Benjamin & Danly 1997 for a discussion of this problem). At $r < r_{\rm cross}$, the density of hot gas is negligible, and so we assume $M_{\rm cld}(r) = M_{\rm cld}(r_{\rm cross})$. Therefore, we compute $M_{\rm cld}(r)$ by solving

$$\frac{dM_{\rm cld}}{dr} = \begin{cases} -A(r)\rho_h(r) & r > r_{\rm cross}\,, \\ 0 & r < r_{\rm cross}\,, \end{cases} \tag{19}$$

subject to the boundary value of $M_{\rm cld}(r_{\rm cross})$. Explicit expressions for $A(r)$ and $M_{\rm cld}(r)$ are given in Appendix C.

3.2. *Cloud Kinematics*

The hot gas surrounding the clouds will exert a drag force opposing their radial infall. Assuming that the drag is caused by momentum imparted to the clouds by hot gas swept up during infall, we find the radial equation of motion to be

$$\frac{d}{dt}\,(M_{\rm cld}\, V_r) = M_{\rm cld}\, g(r)\,, \tag{20}$$

where $g(r)$ is the gravitational acceleration, and the radial velocity, $V_r = -dr/dt$, is positive for infalling bodies. It follows that

$$\frac{dV_r^2}{dr} + \left(\frac{d\ln M_{\rm cld}^2}{dr}\right) V_r^2 = -2g(r) \tag{21}$$

(which corresponds to the case $C_D = 2$ of Benjamin & Danly 1997). The solution to equation (21) is

$$V_r^2(r) = \frac{2}{M_{\rm cld}^2(r)} \int_r^{r_{\rm start}} dr' g(r') M_{\rm cld}^2(r') + V_r^2(r_{\rm start})\,, \tag{22}$$

where we have computed the radial velocity of a cloud that starts to infall from an initial radius $r = r_{\rm start}$ with an initial velocity $V_r(r_{\rm start})$. Note that this expression ignores fragmentation of the clouds due to Kelvin-Helmholtz instabilities, which may be important (Lin & Murray 2000).

To compute $V_r(r)$, we assume that the clouds infall from rest at $r = r_{\rm min}$. As a result, we solve equation (22) with $r_{\rm start} = r_{\rm min}$ and $V_r(r_{\rm start}) = 0$. The resulting $V_r(r)$ are valid in the interval $r = [r_{\rm cross}, r_{\rm min}]$. The solution for $V_r(r_{\rm cross})$ acts as boundary condition in the first of two scenarios we consider for obtaining $V_r(r)$ at $r < r_{\rm cross}$.

In the first scenario, clouds at $r < r_{\rm cross}$ follow pressure-free ballistic trajectories along which $M_{\rm cld}(r) = {\rm const}$. In halos with $r_{\rm cross} < r_{\rm min}$, we solve equation (22) by assuming $r_{\rm start} = r_{\rm cross}$ and let $V_r(r_{\rm start})$ equal the $V_r(r_{\rm cross})$ obtained from the solution at $r > r_{\rm cross}$. For halos with $r_{\rm cross}$ greater than $r_{\rm min}$, we solve equation (22) by assuming $r_{\rm start} = r_{\rm min}$ and $V_r(r_{\rm start}) = 0$; i.e., the clouds undergo ballistic infall from rest at $r = r_{\rm min}$.

In the second scenario, we assume that the cloud kinematics at $r < r_{\rm cross}$ are dominated by random motions. These may be generated by feedback from supernova remnants arising from star formation stimulated in cloud-cloud collisions. Such scenarios have been suggested to solve the "cooling catastrophe" characterizing the hierarchical build up of galaxy-scale structure in most CDM models (White & Frenk 1991). We obtain the velocity dispersion of the clouds by solving the Jeans equations for σ_r, the radial velocity dispersion for a system of clouds with (1) an isotropic velocity distribution, (2) an average density distribution given by $\rho_c(r)$, and (3) the gravitational field of an NFW halo (see eq. [D4] in Appendix D). We then randomly draw the velocities of individual clouds from a Gaussian velocity distribution with dispersion given by σ_r.

We emphasize that our model is most uncertain for low-mass halos. This is because the underlying assumption of pressure equilibrium, which allowed MM to compute the properties of the clouds, breaks down *throughout* the infalling gas for halos with $V_{200} < 100$ km s^{-1}. In these halos the properties of individual clouds are difficult to compute, because without a confining medium the clouds become indistinguishable at $r < r_{\rm cross}$. Our approach to this problem is to assume that the line of sight traverses a medium containing "cloudlike" structures with fixed masses and that these give rise to C IV absorption lines. This assumption needs to tested with high-resolution hydrodynamical simulations of gas at $r < r_{\rm cross}$ that is subject to input of mechanical energy. We have also assumed that equation (17) is valid to obtain the average density of the cool gas in every model. While this expression, which is based on mass conservation for infalling gas, is physically justified in the case of systematic infall, it is arbitrary when the gas kinematics are dominated by random motions. Nevertheless, we believe that the results should provide insights into the observational consequences of random motions (see § 6).

3.3. *Absorption Properties of the Cool Gas*

In order to compute C IV absorption profiles produced by the infalling clouds, we select their locations along the line of sight from the cumulative interception probability function,

$$F(<s) = \frac{\int_{s_{\rm min}}^{s} dy[\rho_c(r(y))/M_{\rm cld}(r(y))]A(r(y))}{\int_{s_{\rm min}}^{s_{\rm max}} dy[\rho_c(r(y))/M_{\rm cld}(r(y))]A(r(y))}\,, \qquad r = \sqrt{y^2 + b^2}\,, \tag{23}$$

where the path integral propagates along a sight line with impact parameter b (where b is the distance in the plane of the sky separating the QSO sight line from the center of the galaxy), $s_{\rm max} = (r_{\rm min}^2 - b^2)^{1/2}$, and $s_{\rm min} = -s_{\rm max}$. We compute $N_{\rm C\,IV}^{\rm cld}(r)$, the C IV column density of a given cloud, from the expression

$$N_{\rm C\,IV}^{\rm cld}(r) = X_{\rm C\,IV}(r) N_{\rm H}^{\rm cld}\,, \tag{24}$$

where the total H column density, i.e., $H^0 + H^+$, of the cloud is given by

$$N_{\rm H}^{\rm cld}(r) = \frac{3\sqrt{2}M_{\rm cld}(r)S}{4\mu m_{\rm H} A(r)}\,, \tag{25}$$

and $X_{\rm C\,IV}(r)$, the ratio of C^{+3} to total hydrogen volume densities, is assumed to depend only on r, the distance of the cloud from the center of the galaxy. To account for variations in $N_{\rm C\,IV}^{\rm cld}$ caused by the variations of sight-line locations across the projected face of the cloud, we have introduced the uniform deviate S, which selects random numbers from the interval $S = (0, \sqrt{2})$. We evaluate $X_{\rm C\,IV}(r)$ by assuming

$$X_{\rm C\,IV}(r) = X_{\rm C\,IV}(R_d)(R_d/r)^{\beta}\,. \tag{26}$$

To determine $X_{\rm C\,IV}(R_d)$ and β, we compute the average C IV column density, $\overline{N}_{\rm C\,IV}(b)$, where

$$\overline{N}_{\rm C\,IV}(b) = \int_{s_{\rm min}}^{s_{\rm max}} ds X_{\rm C\,IV}(r(s))\left[\frac{\rho_c(r(s))}{\mu m_{\rm H}}\right], \qquad r = \sqrt{s^2 + b^2}\,. \tag{27}$$

We find that

$$\overline{N}_{\rm C\,IV}(b) = K\left(\frac{R_d}{b}\right)^{1+\beta}\,, \tag{28}$$

where

$$K = \frac{2C_1}{\mu m_{\rm H}}\frac{X(R_d)}{R_d}\int_0^{x_{\rm max}} \frac{dx}{(1+x^2)^{1+\beta/2}}\,, \tag{29}$$

and where $x_{\rm max} = [(r_{\rm min}/b)^2 - 1]^{1/2}$. We then require the total C IV column density in $n_{\rm cld}$ clouds to agree with $\overline{N}_{\rm C\,IV}(b)$ within some accuracy ϵ, i.e.,

$$\left|\frac{\sum_{i=1}^{n_{\rm cld}} N_{\rm C\,IV}^{\rm cld}(r_i)}{\overline{N}_{\rm C\,IV}(b)} - 1\right| \le \epsilon\,, \tag{30}$$

where $\epsilon = 0.2$ We adjust the input parameters K and β by comparing empirical and model-generated frequency distributions of C IV column densities (see Fig. 6 below), and compute $X(R_d)$ from equation (29).

4. RESULTS OF MONTE CARLO SIMULATIONS: LOW-ION GAS

4.1. *CDM*

Assume the low-ion gas to be in disks with rotation curves normalized to V_{200} at $r = r_{200}$, and V_{200} to be randomly drawn from the distributions in Figure 2. In that case, the kinematics of the low-ion absorption profiles are determined by the form of the rotation curve, $V_{\rm rot}(r)$, the value of the central column density, N_0, and the thickness of the disks, h (see PW97). Because the line width, Δv, increases with h, we follow PW97 by adopting the largest plausible value, $h = 0.3R_d$, in order to maximize Δv. As stated in § 2.3, $V_{\rm rot}(r)$ equals either V_{200} or $f_V V_{200}$. We also make two assumptions about N_0. Either N_0 is equal to the central column density in adiabatically contracted NFW halos, $N_0^{\rm MMW}$, or $N_0 = 10^{21.2}$ cm^{-2}, where the latter value is meant to illustrate scenarios in which star formation has consumed most of the disk gas (the value of R_d does not affect low-ion kinematics, since they are independent of the absolute scale length [PW97]). As a result, the kinematics of the low ions are represented by four independent models. Because each of these will be linked to two kinematic

TABLE 2

DISK-HALO MODELS

	$N_0 = N_0^{\rm MMW}$ or $N_0^{\rm Cor}$ [a]				$N_0 = 10^{21.2}$ cm^{-2}			
	$V_{\rm rot} = V_{200}$		$V_{\rm rot} = f_V V_{200}$		$V_{\rm rot} = V_{200}$		$V_{\rm rot} = f_V V_{200}$	
MODEL	Ballistic	Random	Ballistic	Random	Ballistic	Random	Ballistic	Random
MfVB	...	...	×	...	...	...	...	...
MV2B.....	×	...	...	...	...	...	...	...
MfVR	...	...	...	×	...	...	...	...
MV2R.....	...	×	...	...	...	...	...	...
NfVB.....	...	...	...	...	...	...	×	...
NV2B	...	...	...	...	×	...	...	...
NfVR.....	...	...	...	...	...	...	...	×
NV2R	...	...	...	...	...	×	...	...

[a] Central column density perpendicular to the disk given by equations (3) and (8) for CDM models ($N_0^{\rm MMW}$) and by equation (6) ($N_0^{\rm Cor}$) for TF models

models of the ionized gas (discussed in § 3.2.1), we consider a total of eight kinematic models for each cosmogony. Their properties are summarized in Table 2. The models are designated by four letters; the first, M or N, specifies whether $N_0 = N_0^{\rm MMW}$ or $10^{21.2}$ cm^{-2}; the second, V2 or fV, specifies whether $V_{\rm rot}(r) = V_{200}$ or $f_V V_{200}$; and the third, R or B, indicates whether the velocity field at $r < r_{\rm cross}$ is dominated by random motions or ballistic infall. Thus, the model MV2B has a disk with MMW central column density, disk rotation speed given by V_{200}, and ballistic infall at $r < r_{\rm cross}$. Because the low-ion kinematics of models MfVB, MV2B, NfVB, and NV2B are equivalent to those of models MfVR, MV2R, NfVR, and NV2R, we discuss low-ion results only for the former group.

For a given V_{200}, we find that our single-disk CDM models with $V_{\rm rot}(r) = f_V V_{200}$ result in Δv that are larger than predicted by Kauffmann (1996), who did not correct for the gravitational contributions of the disk or adiabatically contracted halos to the disk rotation curves. Even so, none of our CDM models reproduces the observed low-ion Δv distribution. This is contrary to the expectations of MMW, who conjectured that the higher $V_{\rm rot}(r)$ produced by the more realistic rotation curves would result in a Δv distribution compatible with observations. The reasons this does not occur are illustrated in Figure 2. In every case, the median V_{200} of the intercepted disks is much less than 100 km s^{-1}. Because the Δv predicted for rotating disks typically equals $V_{200}/3$, the predicted median Δv will be much less than 50 km s^{-1}. By contrast, the median Δv of the observed distribution is about 80 km s^{-1}.

Figure 5 shows the results for model NfVB in each CDM cosmogony. With $V_{\rm rot}(r) = f_V V_{200}$ and $N_0 = 10^{21.2}$ cm^{-2}, this model yields the best-case results because it generates the largest Δv of the four models. The larger velocity widths follow (1) from the higher rotation speeds, and (2) because the relatively low central column density of model NfVB results in smaller impact parameters out to the threshold column density N(H I) $= 2 \times 10^{20}$ cm^{-2}, and smaller impact parameters cause larger Δv (PW97). Nevertheless, application of the Kolmogorov-Smirnov (KS) test shows that none of these models is likely to fit the data (see Fig. 5). This conclusion also holds for ICDM, even though ICDM predicts a larger fraction of high-V_{200} halos than the other CDM models. This is because ICDM is also a hierarchical model (Peebles 1999a, 1999b), and as a result a large fraction of the protogalactic mass distribution is in halos with $V_{200} < 100$ km s^{-1}.

4.2. *TF*

In the TF cosmogony, we let N_0 equal either the empirically determined $N_0^{\rm Cor}$ or $10^{21.2}$ cm^{-2}. As discussed previously, $V_{\rm rot}(r) = V_{\rm max}$ in all TF models, where the distribution of $V_{\rm max}$ is shown in Figure 2. Figure 5 also shows the model NfVB results for TF. Here the Δv test yields $P_{\rm KS}(\Delta v) = 0.12$. While lower than the $P_{\rm KS}(\Delta v) = 0.65$ exhibited by models in which every halo has $V_{\rm rot}(r) = 250$ km s^{-1} (PW97), this KS probability is sufficiently large that the more realistic TF model cannot be excluded. We check the robustness of these results for the TF and CDM models in § 6.

5. RESULTS OF MONTE CARLO SIMULATIONS: IONIZED GAS

5.1. *Normalization*

In order to fit the simulations to the data, it is necessary to specify the function $\overline{N}_{\rm C\,IV}(b)$, where b is the impact parameter. This function is crucial, since it constrains kinematic quantities such as $\Delta v_{\rm C\,IV}$ for the C IV profiles by fixing the number of clouds per line of sight (see eq. [30]). We normalize $\overline{N}_{\rm C\,IV}(b)$ by determining the parameters K and β (eqs. [28] and [29]) from comparisons between model and empirically determined frequency distributions of C IV column densities, $f(N_{\rm C\,IV}, z)$. The latter is the product of the number of damped Lyα systems per unit "absorption distance," dn/dX, times $g(N_{\rm C\,IV})$, the conditional distribution of C IV column densities given the presence of a damped Lyα system. We find that

$$f(N_{\rm C\,IV}, z) = \frac{dn}{dz}\left(\frac{dX}{dz}\right)^{-1} g(N_{\rm C\,IV}) ,$$

$$\frac{dX}{dz} = \frac{(1+z)^2}{[(1+z)^2(1+\Omega_M z) - z(z+2)\Omega_\Lambda]^{1/2}} . \qquad (31)$$

Because damped Lyα systems are H I selected, the function g will depend on the differential area of the inclined H I disks giving rise to damped Lyα absorption. As a result, the g will depend on impact parameter, b, and hence on K and β through equations (28) and (29). We adjust K and β by comparing model and empirical $f(N_{\rm C\,IV}, z)$.

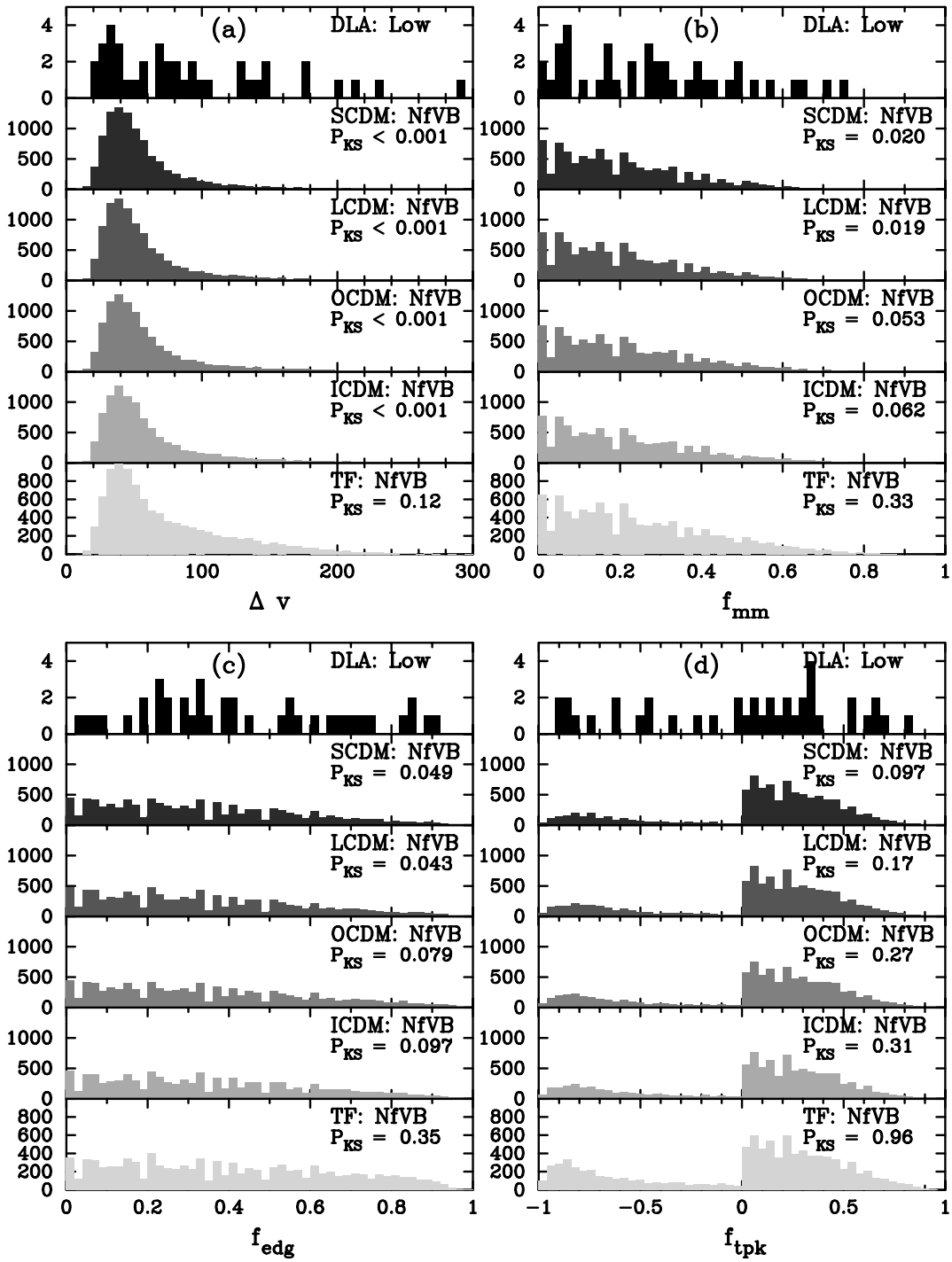

FIG. 5.—Comparison between empirical and Monte Carlo distributions of low-ion test statistics for SCDM, ΛCDM, OCDM, ICDM, and TF cosmogonies. Results are shown for NfVB model compare distributions of (*a*) Δv, (*b*) f_{mm}, (*c*) f_{edg}, and (*d*) f_{tpk} test statistics, which are defined in Paper I. Briefly stated, these quantities are (*a*) the absorption velocity interval, (*b*) the normalized difference between the mean and median velocity, (*c*) the difference between the velocity of the strongest component and the mean velocity, and (*d*) the difference between the velocity of the second-strongest component and the mean velocity. The quantity P_{KS} is the KS probability that model and empirical distributions are drawn from the same parent population.

We constructed the empirical $g(N_{C\,IV})$ from the 32 C IV column densities inferred from the profiles in Figure 1 of Paper I (the actual column densities are reported in Prochaska & Wolfe 1999 and in Lu et al. 1996). To obtain the empirical $f(N_{C\,IV}, z)$, we adopted the ΛCDM model and let $dn/dz = 0.22$, which is appropriate for the mean redshift of this sample. The results are shown as points with error bars in Figure 6. We compare this with the predictions for models MfVB and NfVB in the case of a ΛCDM cosmology. The results are valid for all M and N models, respectively. This is because $f(N_{C\,IV})$ depends on the distribution of impact parameters, but is independent of rotation speed

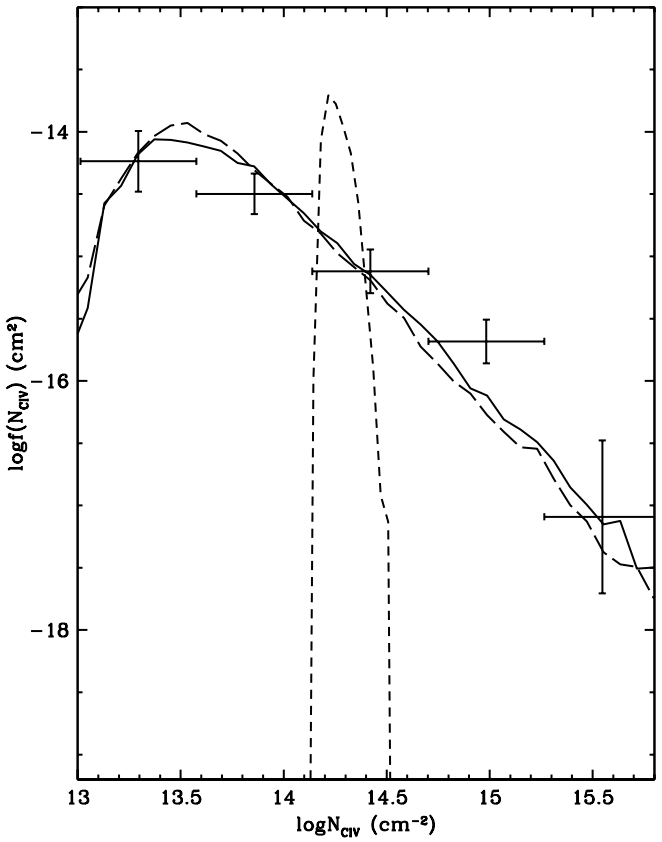

FIG. 6.—Comparison between empirical and model C IV column density distributions. The points with error bars show data. The solid and long-dashed curves show predictions for MfVB and NfVB models, $\beta = 1.5$ and the ΛCDM cosmogony. The short-dashed curve corresponds to the MM model for halos with $V_{200} > 150$ km s^{-1} and in which $\beta \approx -1$.

and infall kinematics. In both classes of models, $\beta = 1.5$ provides a good fit to the data, while $K = 2 \times 10^{15}$ cm^{-2} for model MfVB and 2×10^{14} cm^{-2} for model NfVB. When MM computed $\overline{N}_{\rm C\,IV}(b)$ for cool halo gas photoionized by background radiation, they found K and β to vary with V_{200}, in contrast to our assumption of uniform K and β for halos of all masses. Fortunately, the C IV velocity profiles are independent of K, because both $\overline{N}_{\rm C\,IV}$ and $N^{\rm cld}_{\rm C\,IV}$ are linearly dependent on K, and as a result K drops out of the determination of $n_{\rm cld}$, which is crucial in determining the velocity profile widths (see eq. [30]). On the other hand, the profiles do depend on β. Figure 6 shows that $\beta = -0.9$, which corresponds to the MM results for halos with $V_{200} > 150$ km s^{-1}, results in poor fits to the data. Therefore, the $\beta \approx 1.5$ assumption is consistent with the C IV data and is used in the calculations that follow.

5.2. *Test Statistics*

5.2.1. *CDM Models*

In Figure 7*a* we compare the empirical $\Delta v_{\rm C\,IV}$ distribution with predictions by the ΛCDM cosmogony. We only show results for the case $V_{\rm rot}(r) = V_{200}$, since halo kinematics should be unaffected by disk rotation speed for halos of a given mass. We ignore results for the $f_{\rm mm}$, $f_{\rm edg}$, and $f_{\rm tpk}$ statistics, because in the case of C IV kinematics, $\Delta v_{\rm C\,IV}$ is the most sensitive test statistic for testing any of the models. The principal difference between the distributions in Figure 7*a* stems from the different velocity fields at $r \le r_{\rm cross}$. Models with ballistic infall (MV2B and NV2B) predict larger median $\Delta v_{\rm C\,IV}$ than models with random motions (MV2R and NV2R). For a given N_0, the ballistic models are in slightly better agreement with the data, because the larger $\Delta v_{\rm C\,IV}$ are closer to the observed values.

The value of N_0 also causes differences between the distributions. Comparison between ballistic infall models MV2B and NV2B shows that MV2B predicts lower median $\Delta v_{\rm C\,IV}$ than NV2B. This is because the higher N_0 of model MV2B results in larger impact parameters, which then cause the sight lines to sample the halos at larger radii, where the infall velocities are smaller. In this case, the lower $\Delta v_{\rm C\,IV}$ of the MV2B model is in better agreement with the data. At the same time, model MV2R is in better agreement with the data than NV2R, because the smaller impact parameters predicted by the latter model result in more sight lines traversing the $r \le r_{\rm cross}$ region, where random motions give rise to $\Delta v_{\rm C\,IV}$ that are also lower.

The third difference between the Δv distributions depends on the assumed cosmogony. In Figure 7*b* we use the NfVR model to illustrate the effects of the assumed cosmology. The cosmogonies differ according to the fraction of halos with large V_{200}, a fraction that increases along the SCDM → ICDM sequence. In every cosmogony in this figure, a "spike" in the $\Delta v_{\rm C\,IV}$ distribution at $\Delta v_{\rm C\,IV} = 50$ km s^{-1} is present and increases in strength along the sequence. The spike arises from sight lines traversing the outer regions of high-mass halos at large impact parameters. The high pressure of hot gas in massive halos (see Fig. 3) compresses the clouds, thereby reducing their cross sections. For clouds of fixed mass, the result is an increase in column density. In most cases, only one cloud is required to satisfy equation (30) at large b where $\overline{N}_{\rm C\,IV}$ is small. The spike occurs at $\Delta v_{\rm C\,IV} = 50$ km s^{-1}, because this is the FWHM of the profile caused by a single cloud with an assumed internal velocity dispersion of $\sigma_{\rm int} = 25$ km s^{-1}. In fact, this value of $\sigma_{\rm int}$ was chosen to reproduce the narrowest C IV profiles in our sample.

It is worth noting that despite their differences, most of the models yield large $P_{\rm KS}(\Delta v_{\rm C\,IV})$ values. This is in contrast to tests of low-ion kinematics. In that case, all the $P_{\rm KS}(\Delta v_{\rm low})$ values were too small; i.e., none of the models was compatible with the observed distribution of low-ion Δv. This could imply that while the infall interpretation for the high ions is correct, the disk interpretation for the low ions is incorrect.

5.2.2. *TF Models*

Figure 7*b* also compares the data with the predictions of the TF cosmogony. In this case, V_{200} equals $V_{\rm max}$ or $V_{\rm max}/f_V$, where the $V_{\rm max}$ are the input disk rotation speeds. As a result, the CDM degeneracy of $\Delta v_{\rm C\,IV}$ with respect to disk rotation speed is broken in the TF models. We show results for some examples to illustrate this effect. As expected, the $\Delta v = 50$ km s^{-1} spike is highest for the NV2R model where $V_{200} = V_{\rm max}$. Because of the larger fraction of halos with high V_{200}, the median Δv's are higher than in the CDM models. Agreement with the empirical $\Delta v_{\rm C\,IV}$ distribution improves in the case of random motions at $r < r_{\rm cross}$ and when $V_{200} = V_{\rm max}/f_V$; i.e., with the NfVR model [note that the higher $P_{\rm KS}(\Delta v_{\rm C\,IV})$ value of the NV2R model is an artifact due to the large-amplitude spike at $\Delta v_{\rm C\,IV} = 50$ km s^{-1}], but the $P_{\rm KS}(\Delta v_{\rm C\,IV})$ values are still less than 0.05.

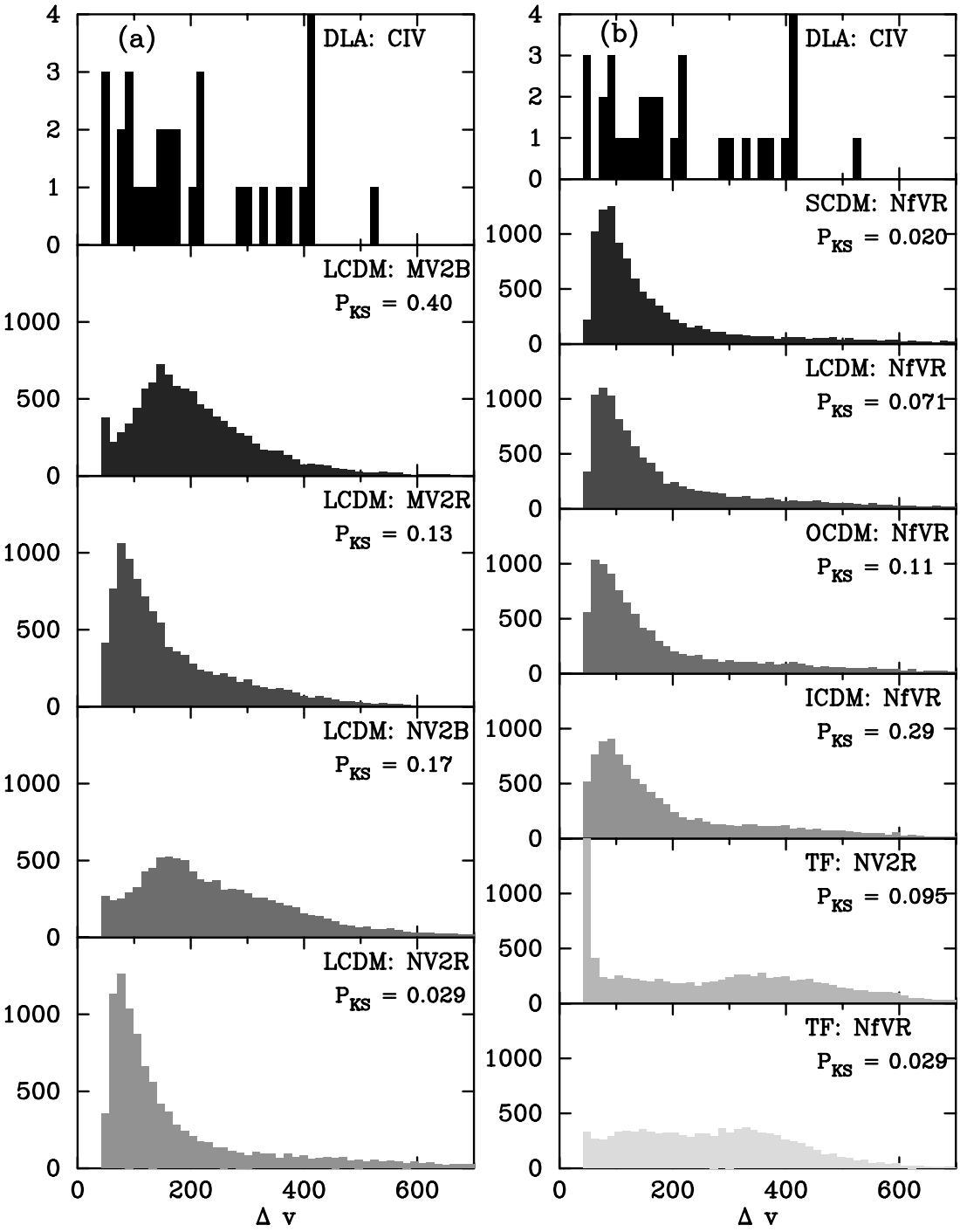

FIG. 7.—Comparison between empirical and Monte Carlo distribution of $\Delta v_{\rm C\,IV}$. (*a*) Results for ΛCDM cosmogony and MV2B, MV2R, NV2B, and NV2R models. (*b*) Results for SCDM through ICDM cosmogonies and NfVR model, and for TF cosmogony with NV2R and NfVR models.

5.3. *Correlation Tests*

In Figure 8, we compare empirical and predicted distributions of δv and $f_{\rm ratio}$. These are the differences between the mean velocities of the C IV and low-ion velocity profiles and the ratio $\Delta v_{\rm C\,IV}/\Delta v_{\rm low}$, respectively. A comparison between empirical and predicted cross-correlation functions for the C IV versus low-ion velocity profiles is also shown.

5.3.1. *δv Test*

In CDM, all the models pass the δv test at more than 83% confidence. In Figure 8*a* we use ΛCDM to illustrate the effects of (1) disk rotation speed, (2) impact parameter, and (3) halo velocity field. Comparison between the MfVB and MV2B models shows that disk rotation speed is the most important effect. Specifically, $P_{\rm KS}(\delta v)$ increases significantly when V_{200} decreases from $f_V V_{200}$ to V_{200}. This behavior is straightforward to explain. In the disk-halo models, the half-width of the δv distribution is roughly equal to the sample average of $V_{\rm rot}(r)$ sin i. This is because the prototypical C IV profile comprises two widely separated absorption components symmetrically displaced about the systemic velocity of the halo. As a result, the mean

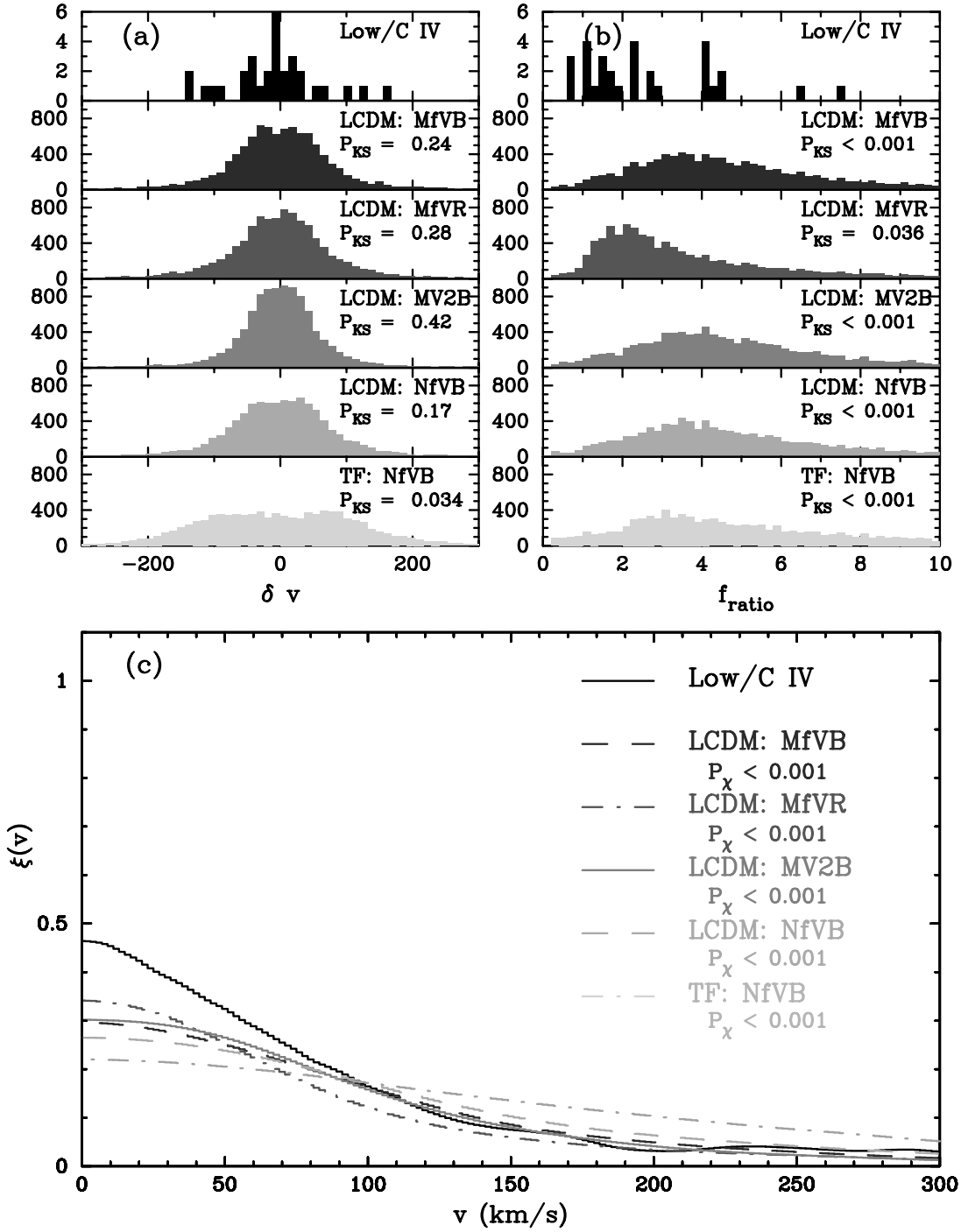

FIG. 8.—Correlation tests. (*a*) Comparison between empirical and Monte Carlo distributions of δv for ΛCDM cosmogony and MfVB, MfVR, MV2B, and NfVB models. The NfVB model is used with the TF cosmogony. (*b*) Same as (*a*), but $f_{\rm ratio}$ is substituted for δv statistic. (*c*) Comparison between empirical and Monte Carlo predictions of $\xi(v)$ for C IV vs. low-ion. Same models as in (*a*) and (*b*) are used. Curves show data (*dark solid curve*), ΛCDM MfVB model (*dark dashed curve*), ΛCDM MfVR model (*dark dot-dashed curve*), ΛCDM MV2B model (*light solid curve*), ΛCDM NfVB model (*light dashed curve*), and TF NfVB model (*light dot-dashed curve*).

velocity of the C IV profile equals the systemic velocity. On the other hand, the low-ion profile consists of multiple contiguous components comprising a single feature that is displaced to either side of the systemic velocity. In this case, the mean velocity of the low-ion profile is separated by $\sim V_{\rm rot}(r) \sin i$ from the systemic velocity. Consequently, the ≈ 75 km s^{-1} half-width of the observed distribution limits the fraction of rapidly rotating disks. This constraint is especially severe for the TF models, in which rotation speeds exceeding 200 km s^{-1} are typical.

On the other hand, the effects of the impact parameter are not as significant. This is because the impact parameter affects the width of the velocity features rather than the location of their velocity centroids. This explains why the MfVB and NfVB results are so similar. Furthermore, the effect of the halo velocity field is even less important, as

shown by comparison between the MfVB and MfVR results. This tells us that for a sufficient number of C IV clouds, the location of the velocity centroid of the C IV profile is independent of whether the clouds are infalling or moving randomly. Therefore, δv is set by the magnitude of $V_{\rm rot}(r)$.

5.3.2. $f_{\rm ratio}$ Test

A natural consequence of the disk-halo hypothesis is the prediction $f_{\rm ratio} \geq 1$. Because the infall velocities of the high ions and the rotation speeds of the low ions occur in the same potential well, they both scale linearly with V_{200}. However, owing to projection effects, the line-of-sight velocity gradients due to radial infall will exceed those due to rotation. Thus, $\Delta v_{\rm C\,IV}$ will be larger than $\Delta v_{\rm low}$. However, the ratios are too large in most CDM models, because of the small $\Delta v_{\rm low}$ and the larger $\Delta v_{\rm C\,IV}$. As a result, the best-case models are those with large $V_{\rm rot}(r)$ for the disks and random motions at $r \leq r_{\rm cross}$ for the halos. The best model is MfVR, as shown in Figure 8*b*. The TF models also produce $f_{\rm ratio}$ that are too high, because in most halos the sight lines intercept the region $r > r_{\rm cross}$, where large infall velocities are present.

5.3.3. *Cross-Correlation Function*

None of the models, neither CDM nor TF, predicts a cross-correlation function with large enough amplitude to fit the data. The reason for this is insufficient overlap in velocity space between the C IV and low-ion profiles. In Figure 8*c*, the best-case model is MfVR, indicating that more overlap occurs when the C IV clouds experience random motions at $r \leq r_{\rm cross}$. Even better agreement is obtained with model MV2R (not shown), implying that overlap increases when the rotation speed of the disk is reduced. This interpretation is supported by the results for the TF models, which exhibit the worst agreement with the data. The TF models predict the largest fraction of halos with high $V_{\rm rot}(r)$ and the lowest fraction of low-mass halos in which random motions dominate the velocity field at $r < r_{\rm cross}$.

5.4. *Model Summary*

In summary, we find the following results for the models we have tested so far:

1. While the extent of the low-ion Δv distribution rules out the single-disk semianalytic CDM models, it is compatible with the TF models (see also Jedamzik & Prochaska 1998).
2. The C IV Δv distribution is compatible with most of the CDM models. In the example shown in Figure 7, the best agreement with the data occurs for models with (1) ballistic infall at $r \leq r_{\rm cross}$ and (2) central disk column densities given by $N_0^{\rm MMW}$. The best agreement with the TF models is for ballistic infall, $N_0 = N_0^{\rm MMW}$, and $V_{200} = V_{\rm max}/f_V$.
3. The δv distribution is compatible with all the CDM models, but is too narrow for the TF models. This is a reflection of the low $V_{\rm rot}(r)$ predicted by CDM and the high $V_{\rm rot}(r)$ predicted by the TF models.
4. Most of the CDM models predict $f_{\rm ratio}$ distributions with median values that are too large. This stems from the low values predicted for $V_{\rm rot}(r)$. The same problem holds for the TF models, but in this case the high $f_{\rm ratio}$ stems from the high values of $\Delta v_{\rm C\,IV}$. In both cosmogonies, some models cannot be ruled out.
5. None of the models predicts C IV versus low-ion cross-correlation functions in agreement with the data.

6. PARAMETER TESTS

The results of the last section can be summarized as follows: When the free parameters of a given model are adjusted to satisfy one test, the model inevitably fails a different test. If this is a generic feature of the disk-halo models, then they may not apply to the damped Lyα systems. This is an important conclusion, and we wish to determine how robust it actually is. Indeed, the models are characterized by several free parameters that are not well determined, and it is possible we have not found the optimal set. For this reason, we now investigate the sensitivity of our conclusions to variations of these parameters.

In a series of trial runs, we found the model kinematics to be most sensitive to three parameters. The first is the central perpendicular column density, N_0. Because the range of impact parameters is limited by N_0, it influences both $\Delta v_{\rm C\,IV}$ and $\Delta v_{\rm low}$. To test the dependence of the kinematics on this quantity, we simulate H I disks with N_0 ranging between $10^{20.8}$ and $10^{22.2}$ cm^{-2}. These values cover the low column densities of the N models and approach the high values of the M models. The second parameter is $V_{\rm cut}$, the low-end cutoff to the distribution of input V_{200} in the CDM models or of input $V_{\rm max}$ in the TF models. The kinematic results should be sensitive to $V_{\rm cut}$, especially in the case of CDM, where it is at the peak of the V_{200} distribution (see Fig. 2). The value used in our models, $V_{\rm cut} = 30$ km s^{-1}, is imposed by thermal expansion of photoionized gas out of the potential wells of halos with V_{200} lower than this (Thoul & Weinberg 1995). However, feedback due to supernova explosions might drive gas out of disks with V_{200} as large as 100 km s^{-1} (see Dekel & Silk 1986; but see also MacLow & Ferrara 1999). For these reasons, we let $V_{\rm cut}$ vary between 30 and 120 km s^{-1}. The third parameter is the C IV column density per cloud, $N_{\rm C\,IV}^{\rm cld}$. The definition given in equations (25)–(27) is for a spherical cloud of a given mass and C^{+3}/H ratio, i.e., $X_{\rm C\,IV}$. To account for deviations from spherical symmetry or from our definition of $X_{\rm C\,IV}$ (see eq. [26]), we introduce the parameter $q_{\rm C\,IV}$, which is the ratio of the true C IV column density to our model definition. We let $q_{\rm C\,IV}$ vary between 0.1 and 1.3. In order to supply the total C IV column density required at a given impact parameter, the number of clouds must increase as $q_{\rm C\,IV}$ decreases. This affects the C IV kinematics, because $\Delta v_{\rm C\,IV}$ will increase with cloud number.

6.1. *CDM*

The results of the parameter tests are summarized in Figure 9, which shows isoprobability contours in the $V_{\rm cut}$ versus N_0 plane. The contours correspond to 0.01, 0.05, and 0.32 for $P_{\rm KS}(\Delta v_{\rm low})$ (Fig. 9*a*), $P_{\rm KS}(\Delta v_{\rm C\,IV})$ (Fig. 9*b*), $P_{\rm KS}(\delta v)$ (Fig. 9*c*), and $P_{\rm KS}(f_{\rm ratio})$ (Fig. 9*d*). We show results for $q_{\rm C\,IV} = 1.0$, since smaller values are found to result in $f_{\rm ratio}$ that are too large. We choose a variant of the NfVR model in which N_0 is a free parameter. We abandon ballistic infall in favor of random motions at $r < r_{\rm cross}$, because we find that random motions produce more overlap in velocity space

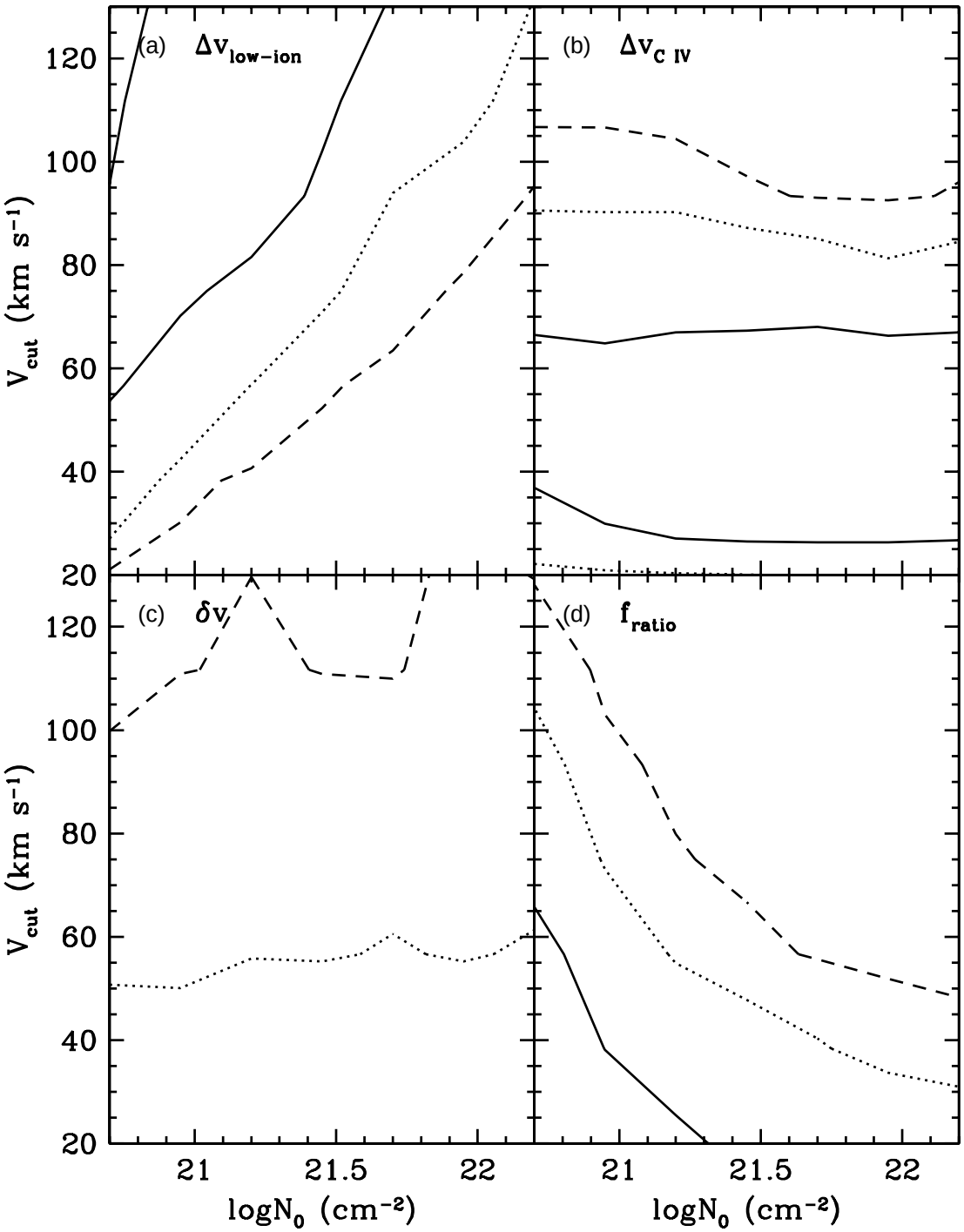

FIG. 9.—Isoprobability contours in V_{cut} vs. N_0 plane resulting from parameter search of ΛCDM cosmogony, where NfVR model is assumed, in which N_0 is a free parameter and where $q_{C\,IV} = 1.0$. Contours correspond to $P_{KS} = 0.32$ (*solid lines*), 0.05 (*dotted lines*), and 0.01 (*dashed lines*). Tests are (*a*) Δv_{low}, (*b*) $\Delta v_{C\,IV}$, (*c*) δv, and (*d*) f_{ratio}.

between low-ion and C IV profiles, and as a result they produce better agreement between model predictions and the empirical test statistics.

Figure 9*a* shows the results for the low-ion Δv test. As expected, models with the standard value $V_{cut} = 30$ km s^{-1} are improbable for reasonable values of N_0. Rather, V_{cut} increases along the $P_{KS}(\Delta v_{low}) = 0.05$ contour from 35 km s^{-1} at log $N_0 = 20.8$ cm^{-2} to 105 km s^{-1} at log $N_0 = 22.0$ cm^{-2}. An increase in N_0 means larger impact parameters, which in turn imply smaller Δv_{low} (see § 5.1). Therefore, an increase in V_{cut} must accompany the increase in N_0 to boost the fraction of high-V_{200} halos required to maintain the extent of the Δv_{low} distribution. By contrast, Figure 9*b* shows that V_{cut} hardly varies with N_0 along the $P_{KS}(\Delta v_{C\,IV})$ contours. In our CDM models, most sight lines traverse halos with low V_{200}, where cloud motions in NfVR models are dominated by random velocities drawn from a Gaussian with a dispersion that is an insensitive function of radius

(eq. [D4]). Consequently, $\Delta v_{\rm C\,IV}$ will be independent of impact parameter and hence independent of N_0. Therefore, $V_{\rm cut}$ need not vary with N_0 to maintain the extent of the $\Delta v_{\rm C\,IV}$ distribution.

Figures 9*c* and 9*d* show the isoprobability contours for the δv and $f_{\rm ratio}$ tests. In Figure 9*c*, none of the contours rise to $P_{\rm KS}(\delta v) = 0.32$ in the $V_{\rm cut}$ versus N_0 plane. The shape of the $P_{\rm KS}(\delta v) = 0.05$ contour has the following implications. First, the insensitivity of the contour to N_0 just indicates that the displacement of the low-ion velocity centroid from the systemic velocity of the galaxy is determined by rotation speed rather than $\Delta v_{\rm low}$. Second, models with $V_{\rm cut} > 55$ km s^{-1} are highly unlikely, since they produce δv that are too large. In Figure 9*d*, N_0 decreases with increasing $V_{\rm cut}$ along all isoprobability contours. Because $\Delta v_{\rm C\,IV}$ increases with increasing $V_{\rm cut}$, N_0 must show a corresponding decrease to boost $\Delta v_{\rm low}$. Otherwise, $f_{\rm ratio}$ becomes larger than observed.

Figure 10 shows the $P_{\rm KS} = 0.05$ contours from the previous figure. The horizontal lines trace out the region in the $V_{\rm cut}$ versus N_0 plane in which $P_{\rm KS} \geq 0.05$ for all four tests; i.e., the parameter space of acceptable models. Physically, the resulting range of $V_{\rm cut}$ (i.e., 35–50 km s^{-1}) is acceptable for models in which gas photoionized by ionizing background radiation escapes from low-mass halos (Thoul & Weinberg 1995; Navarro & Steinmetz 1997). On the other hand, the upper limit on N_0 (i.e., log $N_0 < 21.2$ cm^{-2}) may be too low to explain the shape of the H I column density distribution function (see § 7). Furthermore, this figure indicates that these models may not be viable, since they occupy a small fraction of the depicted parameter space. Note that the horizontal δv contour at $V_{\rm cut} \approx 50$ km s^{-1} is crucial in restricting the acceptable region to such a small area. Because δv is set by rotation speed, we investigated the NV2R models to determine whether the lower rotation speeds would enlarge the acceptable region. The results are shown in Figure 11. As predicted, the lower rotation speeds lift the restricting δv contour from ≈ 50 to ≈ 95 km s^{-1}. However, the lower rotation speeds also increase $f_{\rm ratio}$, with a consequent lowering of the $P_{\rm KS}(f_{\rm ratio})$ contour in Figure 11*d*. Consequently, there is no region in the $V_{\rm cut}$ versus N_0 plane in which all four tests result in $P_{\rm KS} \geq 0.05$ for the NV2R model. Therefore, our conclusion concerning the size of acceptable regions in parameter space appears to be robust.

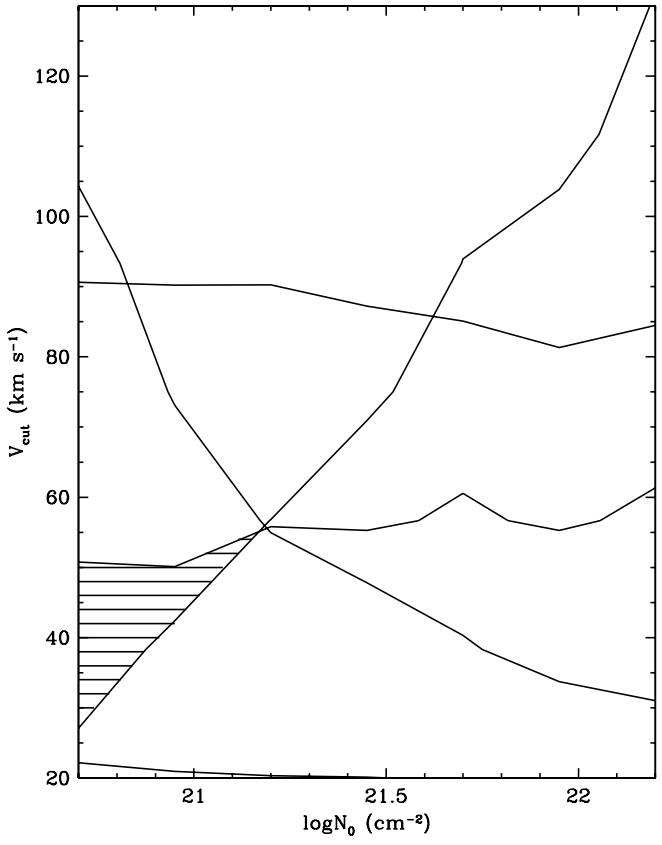

FIG. 10.—Solid lines show contours corresponding to $P_{\rm KS} = 0.05$ in Fig. 9. The region in which $P_{\rm KS} \geq 0.095$ for all four tests is denoted by horizontal lines.

Turning to the cross-correlation function, we find that none of the models within the range of $V_{\rm cut}$ and N_0 depicted in Figure 9 results in C IV versus low-ion cross-correlation functions with acceptable χ^2 values. Apparently, the combination of radial infall and disk rotation produce C IV and low-ion absorption profiles with insufficient overlap in velocity space to explain the data. Better agreement is obtained when log $N_0 > 23$ cm^{-2}. However, column densities this high are ruled out by the other tests. We return to this dilemma in § 7.

In summary, by varying $V_{\rm cut}$, N_0, and $q_{\rm C\,IV}$, we find regions of parameter space in which the ΛCDM models are in better agreement with the data than for the "standard" values of the parameters adopted above. This is especially true for the low-ion Δv test, which ruled out most of the "standard" models (where $V_{\rm cut} = 30$ km s^{-1}). However, the models may still not be viable because of the restricted range of allowable parameters, and because none of the models is compatible with the C IV versus low-ion cross-correlation function.

6.2. *TF*

The corresponding results for the TF models are shown in Figure 12. In this case, the best-fit value of $q_{\rm C\,IV}$ is 1.3. Figure 12*a* illustrates the results for the low-ion Δv test. The figure shows the $P_{\rm KS}(\Delta v_{\rm low}) = 0.05$ contour to enclose a larger area of parameter space than in the CDM case. As in CDM, $V_{\rm cut}$ increases with N_0 along isoprobability contours. However, the $\Delta v_{\rm low}$ contours are less sensitive to $V_{\rm cut}$, because the input halo distribution does not peak at $V_{\rm cut}$, as in CDM (see Fig. 2). Figure 12*b* shows that in contrast to CDM, the $P_{\rm KS}(\Delta v_{\rm C\,IV})$ contours are sensitive functions of N_0. This is because in the TF model, more sight lines traverse high V_{200} halos where C IV clouds undergo infall at $r > r_{\rm cross}$, and as a result $\Delta v_{\rm C\,IV}$ is a sensitive function of impact parameter, and therefore of N_0.

The results for the δv and $f_{\rm ratio}$ tests are plotted in Figures 12*c* and 12*d*. All the models result in $P_{\rm KS}(\delta v) < 0.05$. Clearly, the large fraction of rapidly rotating disks encountered in the TF model produces δv that are too high. By contrast, the results for the $f_{\rm ratio}$ lead to $P_{\rm KS}(\delta v) > 0.05$ throughout the parameter space depicted in the figure, except for the upper right portion, where $P_{\rm KS}(\delta v) > 0.32$. However, part of the improvement here is caused by spikes in the $\Delta v_{\rm C\,IV}$ distribution near 50 km s^{-1}, which prevent $f_{\rm ratio}$ from exceeding observed values when the $\Delta v_{\rm low}$ are small. While the physical basis for such spikes is understood (see § 5.2.1), they have not been confirmed by the data. As in CDM, none of the TF models produces C IV versus low-ion cross-correlation func-

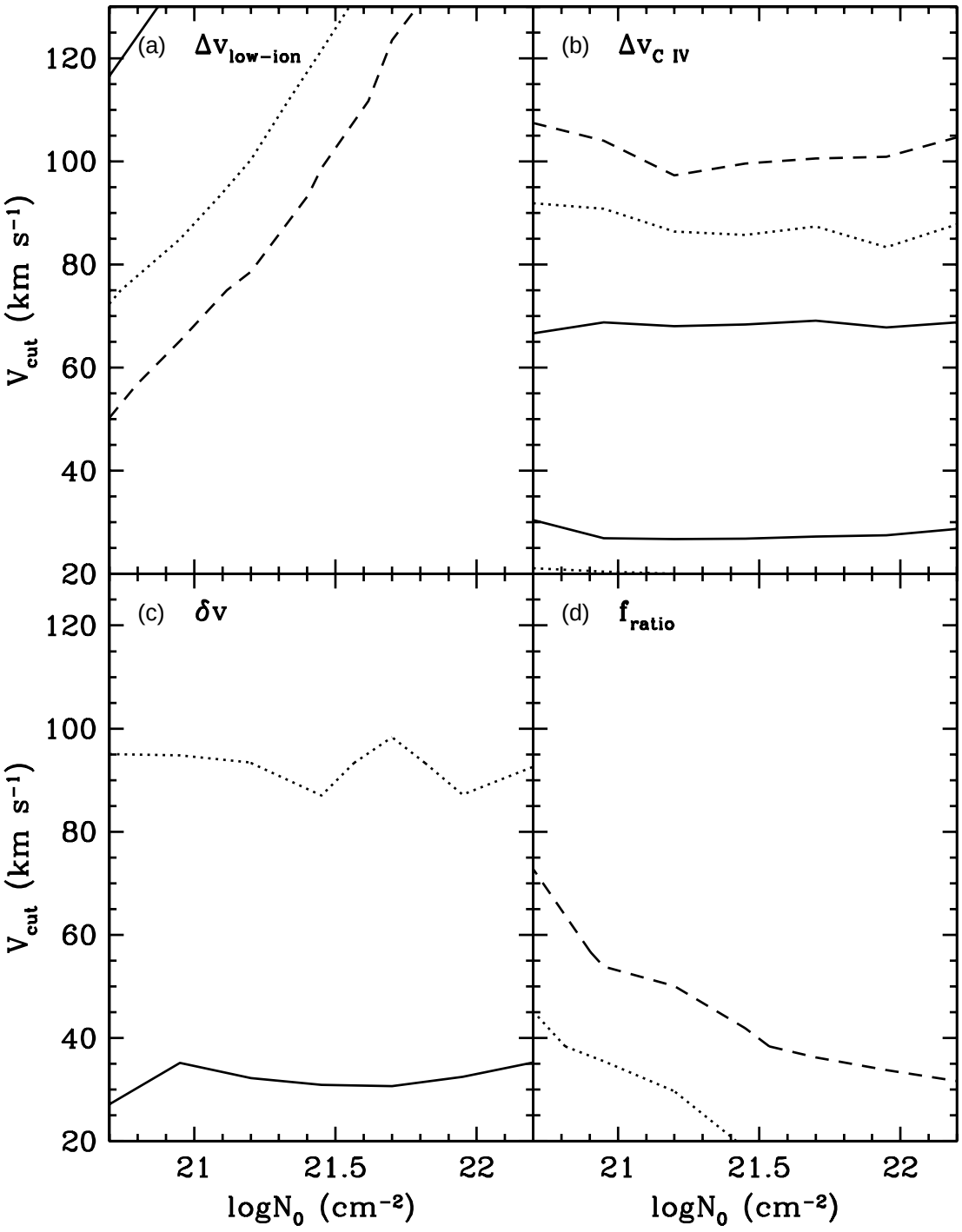

FIG. 11.—Same as Fig. 9, but with NV2R model

tions with acceptable χ^2 values. In fact, the higher fraction of disks with large rotation speeds predicted by the TF model increases the displacement between low-ion and C IV profiles, which produces even lower cross-correlation amplitudes than in the CDM models.

We also tested the sensitivity of the TF model results to variations of (1) γ and V_*, the power-law exponent and fiducial rotation speed in the Tully-Fisher relation (see eq. [13]), and (2) the Schecter function exponent, α (see eq. [15]). Within the parameter range $3 < \gamma < 4$ (cf. Giovanelli et al. 1997; Sakai et al. 2000), the test statistic distributions do not change significantly. In contrast, increasing α above 1.2 reduces Δv_{low} significantly, owing to the larger fraction of low-mass halos. This would occur if the damped Lyα galaxies were drawn from the luminosity function measured for the Lyman-break galaxies (Steidel et al. 1999), since in that case $\alpha = 1.6$ (see § 2.1). Overall, however, the improvement of the model is poor, because f_{ratio} increases to unacceptably high values. The results also change when we vary V_* above 280 km s^{-1} or below 220 km s^{-1}. Yet in both cases, the model does better against some tests and worse against others. In no case did the TF model pass all four tests at more than 95% confidence, nor did the fits of the cross-correlation function become acceptable. In that sense,

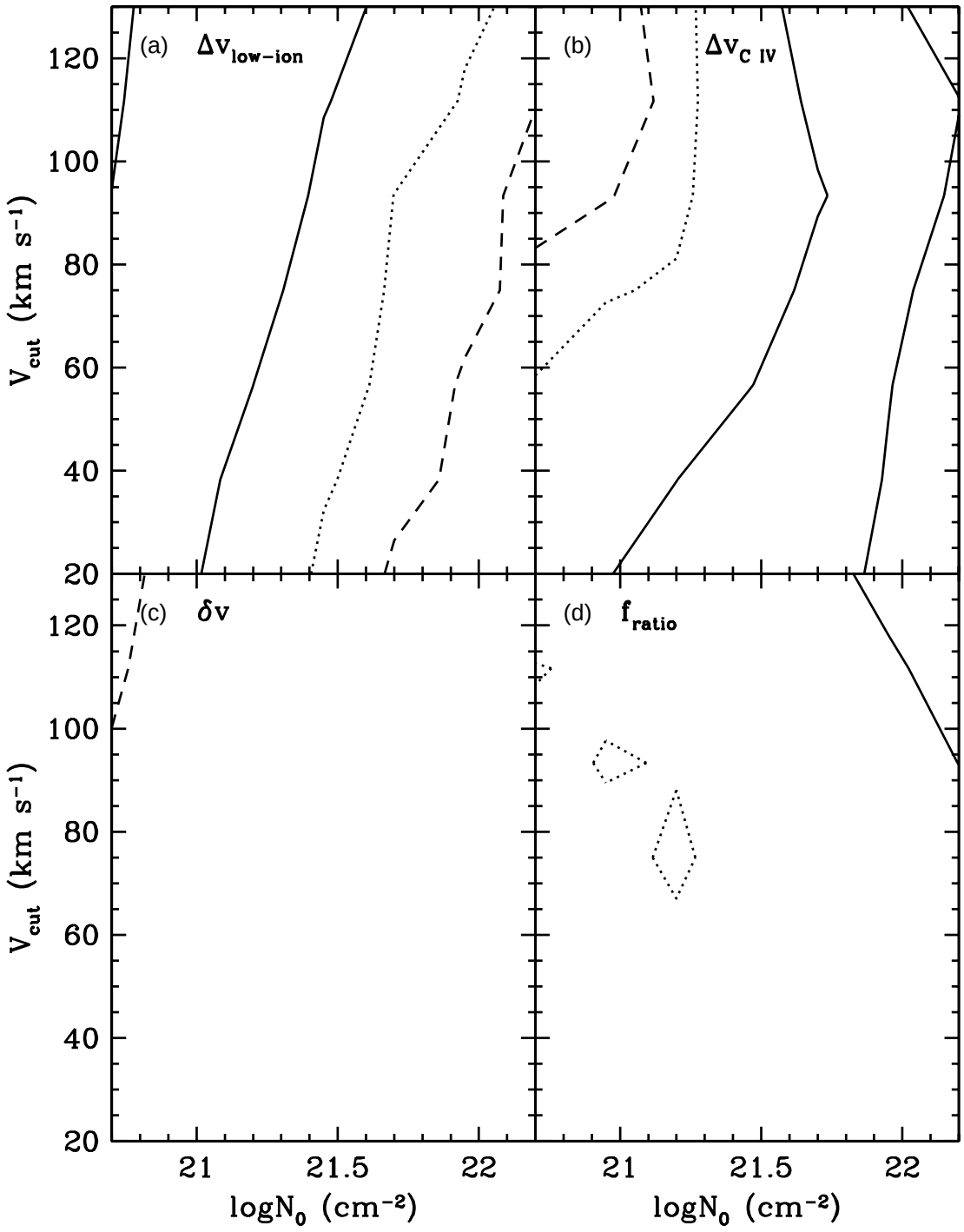

FIG. 12.—Same as Fig. 9, but for TF cosmogony

the TF models are in worse agreement with the data than the CDM models.

7. SUMMARY AND CONCLUDING REMARKS

We used accurate kinematic data acquired for a sample of 35 damped Lyα systems to test the standard paradigm of galaxy formation; i.e., the scenario in which galaxies evolve from the dissipative collapse of virialized gaseous halos onto rotating disks. The data were presented in the form of velocity profiles of high ions, intermediate ions, and low ions in Paper I. In this paper we considered semianalytic models, specifically the MMW models, in which centrifugally supported exponential disks are located at the centers of dark matter halos drawn from mass distributions predicted by standard CDM cosmogonies, and where infall of ionized gas from the halo occurs. We also considered the null hypothesis that current disk galaxies were in place at $z > 3$ (the TF models). We tested the models with Monte Carlo techniques by comparing distributions of test statistics generated from observed and model velocity profiles.

We utilized eight test statistics: $\Delta v_{\rm low}$, $f_{\rm edg}$, $f_{\rm mm}$, and $f_{\rm tpk}$ for the low-ion profiles (see Paper I), $\Delta v_{\rm C\,IV}$ for the C IV profiles, and δv, $f_{\rm ratio}$, and $\xi(v)$ for comparing low-ion and C IV profiles.

First, we discuss the general implications of our work. As discussed in Paper I, velocity profiles overlapping in velocity space in such a way that $\Delta v_{\rm C\,IV} \geq \Delta v_{\rm low}$ are naturally reproduced by scenarios in which low-ion and high-ion kinematic subsystems are in the same gravitational potential well. In the collapse scenario, the velocity fields of both subsystems scale as V_{200}, yet more of V_{200} is projected along the line of sight by gas undergoing radial infall than by gas confined to rotating disks. This was confirmed by our Monte Carlo simulations of the radial infall of ionized gas clouds onto neutral rotating disks. Indeed, in some cases the infall velocities exceed V_{200}, resulting in $\Delta v_{\rm C\,IV}/\Delta v_{\rm low}$ ratios that are too large. By contrast, scenarios in which the high ions are embedded in gaseous outflows (e.g., Nulsen, Barcons, & Fabian 1998), or any flows not generated by dark matter potentials determining low ion velocities, will in general not satisfy these constraints.

Next, we discuss specific conclusions arising from this work, in particular the results of model testing. Tests of models with the *standard* parameters discussed in § 4 and § 5 led to the following conclusions:

1. In the case of the low-ion gas, none of measured distributions of $\Delta v_{\rm low}$, $f_{\rm edg}$, $f_{\rm mm}$, and $f_{\rm tpk}$ was compatible with the predictions of the CDM cosmogonies at the 95% confidence level. By comparison, the TF model was compatible with the data at the 88% confidence level.

2. For the high-ion gas, we considered only the $\Delta v_{\rm C\,IV}$ distribution. Comparison with the data showed CDM models with the high column densities predicted by MMW, i.e., $N_0 = N_0^{\rm MMW}$, were in good agreement with the data. CDM models with significantly lower N_0 were not as good, because they produced overly large $\Delta v_{\rm C\,IV}$. For the same reasons, TF models with high N_0 were in better agreement with the data than those with low N_0.

3. To test model predictions for the relative properties of the high- and low-ion gas, we considered the δv distribution. The CDM models were compatible with the data, while TF models were not. Apparently, the high rotation speed TF disks displace the asymmetric low-ion profiles too far from the velocity centroids of the C IV profiles.

4. Tests of the $f_{\rm ratio}$ distributions showed that neither CDM nor TF model predictions agreed with the data at 95% confidence.

5. Neither the CDM nor TF models predicted C IV versus low-ion cross-correlation functions that were compatible with the data at 99% confidence.

We then explored parameter space to determine whether these conclusions were robust (see § 6). We varied three crucial parameters: $V_{\rm cut}$, N_0, and $q_{\rm C\,IV}$. This exercise led to the following conclusions:

6. Figure 9 shows that the NfVR-ΛCDM model is compatible with the $\Delta v_{\rm low}$, $\Delta v_{\rm C\,IV}$, δv, and $f_{\rm ratio}$ tests at more than 95% confidence throughout the small area of the $V_{\rm cut}$ versus N_0 plane shown in Figure 10. This is a serious shortcoming, since the NfVR model used for the comparison is "optimistic," in that it predicts a constant velocity rotation curve with maximum rotation speed $V_{\rm rot}(r) = f_V V_{200}$. It also predicts low impact parameters, owing to the low value of $N_0 = 10^{21.2}$ cm^{-2}. In addition, a small decrease in disk thickness would eliminate consistency throughout parameter space; i.e., the disks must be thick.

7. Figure 12 shows the NfVR-TF model to be compatible with the $\Delta v_{\rm low}$, $\Delta v_{\rm C\,IV}$, and $f_{\rm ratio}$ tests and incompatible with the δv test at 95% confidence.

8. Neither CDM nor TF models produce C IV versus low-ion cross-correlation functions that were consistent with the data in the parameter space shown in these figures.

What have we learned from the model tests? Because the CDM models pass four out of five tests and the TF models pass three out of five tests, the CDM models appear to be more plausible. However, to achieve this result it was necessary to adopt a flat rotation curve with $V_{\rm rot}(r) = f_V V_{200}$. This is the maximum rotation speed possible for a model disk, and $V_{\rm rot}(r)$ in realistic protogalactic disks are probably lower. However, Figure 11 shows that a parameter search for models with $V_{\rm rot}(r) = V_{200}$ reveals no region in parameter space that is compatible with the four kinematic tests at 95% confidence. Second, the limit $N_0 < 10^{21.2}$ cm^{-2} indicates that exponential disk models should predict a steepening of the column density distribution function at $N > 10^{21.2}$ cm^{-2}. This effect is not present in the data (Wolfe et al. 1995; Rao & Turnshek 1999). Third, the failure of any model to reproduce the C IV versus low-ion $\xi(v)$ indicates that significant overlap in velocity space between the low- and high-ion velocity fields was not achieved. Fourth, the CDM models predict that most of the damped Lyα systems occur in low-mass halos, where the kinematic state of the ionized gas is highly uncertain (see § 3.1).

Does this mean that disk-halo models for damped Lyα systems are ruled out? We think it is premature to reach this conclusion. Rather, we take these results to mean that if the collapse scenario is correct, a stronger coupling between the kinematic subsystems is required. One possibility that comes to mind is for low ions to be associated with the infalling C IV clouds. This would increase the low-ion line-of-sight velocities and cause smaller differences between the C IV and low-ion velocity profiles. However, the problem remains that there is no evidence for low ions with high-ion kinematics. Another way to couple the subsystems is to include the angular momentum of the halo gas. This is neglected in the radial infall model. As the C IV clouds approach the disk, they spin up and experience azimuthal velocity components approaching $V_{\rm rot}(r)$. The idea is plausible if the angular momentum vector of the infalling gas is related to that of the disk, and if clouds near the disk are likely to be detected. It is encouraging that recent N-body simulations show the angular momenta of disk and halo to be correlated (D. Weinberg 2000, private communication). It is also encouraging that the density of clouds along the line of sight is highest near the disk. Still, if this idea does not work, one would be forced to abandon the disk-halo hypothesis, i.e., one of the standard paradigms of galaxy formation.

Can the kinematic data be better explained by scenarios other than infall of ionized gas onto rotating disks of neutral gas? First, we already discussed problems associated with outflow models. Second, lacking analytic expressions for the various quantities, it is not clear whether numerical simulations of damped Lyα systems are compatible with the kinematics of the ionized gas. However, the density contours in Haehnelt, Steinmetz, & Rauch (1998)

show the C IV clouds to be within ~ 10 kpc of the low-ion clouds, in which case both would be subjected to the same dark matter gravitational field. Because the low-ion gas is not confined to rotating disks, it is not obvious why the predicted $f_{\rm ratio}$ should exceed the observed lower limit of unity. To satisfy this constraint, one must consider contributions to the C IV profiles from gas outside the dark matter halos, perhaps in the fashion described by Rauch, Haehnelt, & Steinmetz (1997) for the C IV QSO absorption lines. Third, the scenario described by the semianalytic modeling of Maller et al. (2000) may provide a good fit to the C IV kinematics. In particular, both the low-ion and C IV kinematics arise from the orbital motions of mini-halos accreted onto more massive halos with $V_{200} \sim 150$ km s^{-1}, implying $\Delta v_{\rm C\,IV} \geq \Delta v_{\rm low}$ and that C IV and low-ion profiles are well correlated. The current difficulty with the model is to physically motivate the very large Mestel disks required to explain the low-ion kinematics. In any case, performing the tests outlined in this paper will reveal how robust these models actually are.

We wish to thank the following people for valuable discussions: Robert Benjamin, James Bullock, Eric Gawiser, Chris McKee, Jim Peebles, Martin Rees, and Amos Yahil. J. X. P. acknowledges support from a Carnegie postdoctoral fellowship. A. M. W. was partially supported by NSF grant AST 00071257.

APPENDIX A

PRESS-SCHECTER THEORY FOR ICDM COSMOGONIES

According to Press-Schecter theory, the density of bound halos in the mass interval $(M, M + dM)$ is given by

$$n(M, z)dM = -2\,\frac{\rho}{M}\,\frac{\partial F}{\partial M}\,dM\,, \tag{A1}$$

where ρ is the mean density of matter and F is the fraction of objects with masses $\leq M$ that collapsed by redshift z. For Gaussian-distributed density fields, F is given by

$$F = \frac{1}{2}\left[1 - {\rm erf}\left(\frac{\delta_c}{\sqrt{2}D(z)\Delta_0(M)}\right)\right], \tag{A2}$$

where $D(z)$ is the density-contrast growth factor (Peebles 1980), and $\Delta_0(M)$ is the current rms density contrast with mass M. While equation (A2) is applicable to ACDM models, it does not apply to ICDM models, where the density contrasts are not Gaussian distributed. Rather, we use an analytic fit to results of numerical computations (Peebles 1998b), which shows that in ICDM, F is given by

$$F = 0.37\,\exp\left[-0.67\,\frac{\delta_c}{D(z)\Delta_0(M)}\right]. \tag{A3}$$

For power spectra in which $P(k) \propto k^n$, $\Delta_0(M) \propto M^{-(n+3)/6}$. As a result,

$${\rm ICDM:n}(M, z)dM = 0.5\,\frac{\rho}{M}\left(\frac{M}{M_*}\right)^{(n+3)/6}\exp\left[-0.67\left(\frac{M}{M_*}\right)^{(n+3)/6}\right]\frac{n+3}{6}\,\frac{dM}{M}\,, \tag{A4}$$

where M_*, the mass going nonlinear at redshift z, is obtained from the expression $\Delta_0(M_*) = \delta_c/D(z)$ (see White 1996). One finds that

$$M_*(z) = M_8\left[\frac{\Delta_0(M_8)}{\delta_c}\right]^{6/(n+3)}\left[D(z)\right]^{6/(n+3)}\,, \tag{A5}$$

where the mass in a sphere with radius $R = 8\,h^{-1}$ Mpc, $M_8 = 5.9 \times 10^{14}\Omega_M\,M_\odot$. Throughout the paper, we denote $\Delta_0(M_8)$ by the more conventional symbol, σ_8. In the case of Gaussian linear density fields applicable to ACDM models, we have

$${\rm ACDM:n}(M, z)dM = -\sqrt{\frac{2}{\pi}}\,\frac{\rho}{M}\,\frac{\delta_c}{D\Delta_0^2}\,\frac{d\Delta_0}{dM}\,\exp\left(-\frac{\delta_c^2}{2D^2\Delta_0^2}\right)dM\,, \tag{A6}$$

where in this case $\Delta_0(M)$ is determined by the full CDM power spectrum (Bardeen et al. 1986).

APPENDIX B

HOT GAS IN NFW HALOS

Following MM, we assume that the hot gas is in hydrostatic equilibrium with the dark matter potential and exhibits adiabatic temperature and density profiles out to $r_{\rm min} = \min\,(r_{\rm cool}, r_{200})$. For the NFW rotation curves given in equation (7),

the density and temperature profiles of hot gas within $r_{\rm min}$ are given by

$$\rho_h(r) = \rho_h(r_{\rm min})[1 + 0.8Z_{\rm NFW}(r)]^{3/2}, \qquad T_h(r) = T_h(r_{\rm min})[1 + 0.8Z_{\rm NFW}(r)], \qquad 0 < r < r_{\rm min}\,, \tag{B1}$$

where

$$Z_{\rm NFW}(r) = \frac{c}{\delta_{\rm NFW}}\left[\frac{\ln(1+x)}{x} - \frac{\ln(1+x_{\rm min})}{x_{\rm min}}\right], \qquad x = \frac{r}{r_s}\,, \tag{B2}$$

and

$$\delta_{\rm NFW} = \left[\ln(1+c) - \frac{c}{1+c}\right]. \tag{B3}$$

At $r > r_{\rm min}$, the hot gas either follows isothermal profiles, when $r_{200} > r_{\rm cool}$, or does not exist, when $r_{200} < r_{\rm cool}$. The temperature and density of hot gas at $r_{\rm min}$ are given by

$$T_h(r_{\rm min}) = T_{\rm vir} \tag{B4}$$

and

$$\rho_h(r_{\rm min}) = \frac{f_g V_{200}^2}{4\pi G r_s^2}\,\frac{c}{\delta_{\rm NFW}}\,\frac{1}{x_{\rm cool}(1+x_{\rm cool})^2}\,, \qquad x_{\rm cool} = \frac{r_{\rm cool}}{r_s}\,, \tag{B5}$$

where f_g is the mass fraction in gas. To solve for $r_{\rm cool}$, we follow MM and let $\rho_h(r_{\rm min}) = 5(\mu m_{\rm H})^2 V_{200}{}^2/4\Lambda(T_{\rm vir})t_M$, where $\Lambda(T)$ is the cooling function. From the last equation, we find that $x_{\rm cool}$ is the root of the polynomial

$$x_{\rm cool}(1+x_{\rm cool})^2 - \frac{c}{\delta_{\rm NFW}}\left(\frac{R_{\rm cool}}{r_s}\right)^2 = 0\,, \tag{B6}$$

where $R_{\rm cool}$, the cooling radius of a singular isothermal sphere, is given by

$$R_{\rm cool} = \left[\frac{\Lambda(T_v)t_M\, m_d}{5\pi G\mu^2 m_{\rm H}^2}\right]^{1/2} \tag{B7}$$

(see MM). The root of interest is given by $x_{\rm cool} \geq 1$.

APPENDIX C

COOL GAS

The cool gas in the halo comprises photoionized clouds formed from hot-phase gas at $r \leq r_{\rm min}$, where $r_{\rm min} = \min(r_{\rm cool}, r_{200})$. Therefore, the mass of gas in the cool phase is given by

$$M_{\rm cool} = f_g M(r_{\rm min}) - M_h(r_{\rm min})\,, \tag{C1}$$

where $M(r_{\rm min})$, the total mass within $r_{\rm min}$, and $M_h(r_{\rm min})$, the mass of hot gas within $r_{\rm min}$, are given by

$$M(r_{\rm min}) = \frac{r_{\rm min} V_{\rm rot}^2(r_{\rm min})}{G} \tag{C2}$$

and

$$M_h(r_{\rm min}) = \int_0^{r_{\rm min}} 4\pi r^2 \rho_h(r)\, dr\,. \tag{C3}$$

For NFW halos, we use the rotation curve in equation (7) to relate $V_{\rm rot}(r_{\rm min})$ to V_{200}, equations (B1)–(B4) to compute the integral in equation (C3), and finally equation (B5) to evaluate $\rho_h(r_{\rm min})$. The result is

$$M_{\rm cool} = \frac{f_g r_{200} V_{200}^2}{G\delta_{\rm NFW}}\left[\ln(1+x_{\rm min}) - \frac{x_{\rm min}}{(1+x_{\rm min})} - \frac{I_{\rm NFW}(x_{\rm min})}{(x_{\rm cool})(1+x_{\rm cool})^2}\right], \qquad x = \frac{r}{r_s}\,, \tag{C4}$$

where

$$I_{\rm NFW}(x_{\rm min}) = \int_0^{x_{\rm min}} x^2[1 + 0.8Z_{\rm NFW}(x)]\, dx\,. \tag{C5}$$

MM assume the following form for the density of the cool gas:

$$\rho_c(r) = \frac{M_{\rm cool}}{4\pi r^2 V_c\, t_M}\,, \tag{C6}$$

where V_c is a characteristic infall velocity. Combining the last equation with $\rho_c(r) = C_1/r^2$, we have

$$C_1 = \frac{f_g r_{200} V_{200}^2}{4\pi G V_c t_M \delta_{\rm NFW}} \left[\ln(1 + x_{\rm min}) - \frac{x_{\rm min}}{(1 + x_{\rm min})} - \frac{I_{\rm NFW}(x_{\rm min})}{(x_{\rm cool})(1 + x_{\rm cool})^2} \right]. \tag{C7}$$

Having obtained C_1, we compute $r_{\rm cross}$ by combining these results with equation (17). We find $r_{\rm cross}$ to be the roots of the following equation:

$$r^2[1 + Z_{\rm NFW}(r)]^{5/2} - \frac{C_1 T_c}{\rho_h(r_{\rm min}) T_h(r_{\rm min})} = 0 . \tag{C8}$$

We compute the cloud cross section, $A(r)$, by combining these results with equation (18). We find that

$$A(r) = \pi \begin{cases} C_2 M_{\rm cld}^{2/3}(r)[1 + Z_{\rm NFW}(r)]^{-5/3} & r > r_{\rm cross} , \\ C_3 M_{\rm cld}^{2/3}(r_{\rm cross})(r/r_{\rm min})^{4/3} & r < r_{\rm cross} , \end{cases} \tag{C9}$$

where

$$C_2 = \left[\frac{3T_c}{4\pi\rho_h(r_{\rm min}) T_h(r_{\rm min})} \right]^{2/3}, \qquad C_3 = \left(\frac{3r_{\rm min}^2}{4\pi C_1} \right)^{2/3} . \tag{C10}$$

We compute the cloud mass by integrating equation (19) from $r_{\rm min}$ to r to find $M_{\rm cld}(r)$ at $r > r_{\rm cross}$, and assume $M_{\rm cld}(r) = M_{\rm cld}(r_{\rm cross})$ at $r < r_{\rm cross}$. We find that

$$M_{\rm cld}(r) = \begin{cases} M_{\rm cld}(r_{\rm min}) \left\{ 1 + \dfrac{\pi\rho_h(r_{\rm min}) C_2 r_s}{3M_{\rm cld}^{1/3}(r_{\rm min})} \displaystyle\int_{r/r_s}^{r_{\rm min}/r_s} [1 + 0.8 Z_{\rm NFW}(x)]^{-1/6}\, dx \right\}^3 & r > r_{\rm cross} , \\ M_{\rm cld}(r_{\rm cross}) & r < r_{\rm cross} . \end{cases} \tag{C11}$$

APPENDIX D

CLOUD KINEMATICS

The infall velocities of the clouds are computed as follows. At $r > r_{\rm cross}$ we compute $V_r(r)$ from equation (22) by using the solutions for $M_{\rm cld}(r)$ given in Appendix C and noting that the gravitational acceleration is given by $g(r) = V_{\rm rot}^2(r)/r$. From equation (7), we find

$$g(r) = V_{200}^2 \frac{1}{r_s} \frac{c}{\delta_{\rm NFW}} \frac{1}{x^2} \left[\ln(1 + x) - \frac{x}{1 + x} \right], \qquad x = \frac{r}{r_s} . \tag{D1}$$

At $r < r_{\rm cross}$ we consider two scenarios. In the case of ballistic infall, we assume $M_{\rm cld}(r) = {\rm const}$. For clouds with infall velocity $V_r(r_{\rm cross})$ at $r = r_{\rm cross}$, the ballistic solution for NFW halos is given by

$$V_r^{\rm bal}(x) = \sqrt{V_r^2(r_{\rm cross}) + V_{200}^2 \frac{2c}{\delta_{\rm NFW}} \left[\frac{\ln(1 + x)}{x} - \frac{\ln(1 + x_{\rm cross})}{x_{\rm cross}} \right]}, \qquad x = \frac{r}{r_s} . \tag{D2}$$

In the case where the kinematics are dominated by random motions, we solve the Jeans equations for $\sigma_r(r)$, the radial velocity dispersion of the clouds, assuming locally isotropic velocity dispersions (Binney & Tremaine 1987). In this case, we have

$$\sigma_r(r)^2 = \frac{1}{\nu(r)} \int_r^\infty dx\, \nu(x) g(x) , \tag{D3}$$

where $\nu(r)$ is the average density of clouds. Assuming $\nu(r) \propto \rho_c(r)$, we find that

$$\sigma_r^2(r) = V_{200}^2 \frac{c}{3\delta_{\rm NFW}} \left[\left(\frac{1}{x} - 2x^2 \right) \ln(1 + x) + 2x^2 \ln x + 2x - 1 \right], \qquad x = \frac{r}{r_s} . \tag{D4}$$

REFERENCES

Bardeen, J. M., Bond, J. R., Kaiser, N., & Szalay, A. S. 1986, ApJ, 304, 15
Barnes, J., & Efstathiou, G. 1987, ApJ, 319, 575
Benjamin, R. A., & Danly, L. 1997, ApJ, 481, 764
Binney, J., & Tremaine, S. 1987, Galactic Dynamics (Princeton: Princeton Univ. Press), 198
Blumenthal, G. R., Faber, S. M., Flores, R., & Primack, J. R. 1986, ApJ, 301, 27
Courteau, S. 1996, ApJS, 103, 363
Courteau, S. 1997, AJ, 114, 2402
Dekel, A., & Silk, J. 1986, ApJ, 303, 39
Fabian, A. 1994, ARA&A, 32, 277
Giovanelli, R., Haynes, M. P., da Costa, L. N., Freudling, W., Salzer, J. J., & Wegner, G. 1997, ApJ, 477, L1
Gonzalez, A. H., Williams, K. A., Bullock, J. S., Kolatt, T. S., & Primack, J. R. 2000, ApJ, 528, 145
Haehnelt, M. G., Steinmetz, M., & Rauch, M. 1998, ApJ, 495, 647

Jedamzik, K., & Prochaska, J. X. 1998, MNRAS, 296, 430
Kauffmann, G. 1996, MNRAS, 281, 475
Kepner, J. V., Babul, A., & Spergel, D. N. 1997, ApJ, 487, 61
Lin, D. N. C., & Murray, S. D. 2000, ApJ, 540, 170
Loveday, J., Tresse, L., & Maddox S. 1999, MNRAS, 310, 281
Lu, L., Sargent, W. L. W., Barlow, T. A., Churchill, C. W., & Vogt, S. 1996, ApJS, 105, 475
Mac Low, M.-M., & Ferrara, A. 1999, ApJ, 513, 142
Maller, A. H., Prochaska, J. X., Somerville, R. S., & Primack, J. 2000, preprint (astro-ph/0002449)
Mo, H. J., Mao, S., & White, S. D. M. 1998, MNRAS, 295, 319 (MMW)
Mo, H. J., & Miralda-Escudé, J. 1996, ApJ, 469, 589 (MM)
Navarro, J. F., Frenk, C. S., & White, S. D. M. 1997, ApJ, 490, 493 (NFW)
Navarro, J. F., & Steinmetz, M. 1997, ApJ, 478, 13
Nulsen, P. E. J., Barcons, X., & Fabian, A. C. 1998, MNRAS, 301, 168
Peebles, P. J. E. 1980, The Large-Scale Structure of the Universe (Princeton: Princeton Univ. Press), 49
———. 1999a, ApJ, 510, 523
Peebles, P. J. E. 1999b, ApJ, 510, 531
Prochaska, J. X., & Wolfe, A. M. 1997, ApJ, 487, 73 (PW97)
———. 1998, ApJ, 507, 113 (PW98)
———. 1999, ApJS, 121, 369
Rao, S. M., & Turnshek, D. A. 1999, preprint (astro-ph/9909164)
Rauch, M., Haehnelt, M. G., & Steinmetz, M. 1997, ApJ, 481, 601
Rees, M. J., & Ostriker, J. P. 1977, MNRAS, 179, 541
Sakai, S., et al. 2000, ApJ, 529, 698
Steidel, C. C., Adelberger, K. L., Giavalisco, M., Dickinson, M., & Pettini, M. 1999, ApJ, 519, 1
Thoul, A. A., & Weinberg, D. H. 1995, ApJ, 442, 480
White, S. D. M. 1996, in Cosmology and Large Scale Structure, ed. R. Schaeffer et al. (Amsterdam: Elsevier), 349
White, S. D. M., & Frenk, C. S. 1991, ApJ, 379, 52
Wolfe, A. M., Lanzetta, K. M., Foltz, C. B., & Chaffee, F. H. 1995, ApJ, 454, 698
Wolfe, A. M., & Prochaska, J. X. 2000, ApJ, 545, this issue (Paper I)